A TRIDENT SCHOLAR PROJECT REPORT

NO. 499

The Effects of Acceleration on Film Cooling in Gas Turbine Engines

by

Midshipman 1/C Clayton S. Pelzer, USN

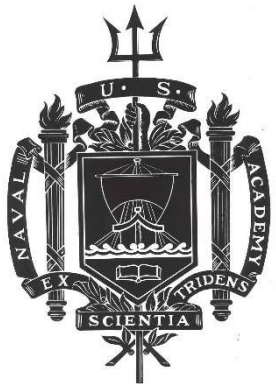

UNITED STATES NAVAL ACADEMY
ANNAPOLIS, MARYLAND

USNA-1531-2

REPORT DOCUMENTATION PAGE

Form Approved
OMB No. 0704-0188

1. REPORT DATE *(DD-MM-YYYY)*	**2. REPORT TYPE**	**3. DATES COVERED** *(From - To)*
7/6/20		

4. TITLE AND SUBTITLE
The Effects of Acceleration on Film Cooling in Gas Turbine Engines

5a. CONTRACT NUMBER

5b. GRANT NUMBER

5c. PROGRAM ELEMENT NUMBER

6. AUTHOR(S)
Pelzer, Clayton S.

5d. PROJECT NUMBER

5e. TASK NUMBER

5f. WORK UNIT NUMBER

7. PERFORMING ORGANIZATION NAME(S) AND ADDRESS(ES)

8. PERFORMING ORGANIZATION REPORT NUMBER

9. SPONSORING / MONITORING AGENCY NAME(S) AND ADDRESS(ES)
U.S. Naval Academy
Annapolis, MD 21402

10. SPONSOR/MONITOR'S ACRONYM(S)

11. SPONSOR/MONITOR'S REPORT NUMBER(S)
Trident Scholar Report no. 499 (2020)

12. DISTRIBUTION / AVAILABILITY STATEMENT

This document has been approved for public release; its distribution is UNLIMITED.

13. SUPPLEMENTARY NOTES

14. ABSTRACT

Gas turbine engine blades contain film cooling holes that direct cool air over the surface of the blades, protecting them from high temperatures up to 2000 °C inside the turbines. There are many factors that affect film cooling, but one of the most important is the acceleration of flow over the surface of the blade. Its impacts on the film cooling process are not fully understood. Previous experiments have compared film cooling both with and without accelerating flow, but no study has reported on heat transfer and flow with different levels of acceleration. In order to understand the direct effects of acceleration, a test section was constructed to model the interactions of flow over a gas turbine blade by matching dimensionless parameters. The test section has lower temperatures and larger dimensions than an actual turbine blade, physically allowing for direct observation. The values determined through this work should give blade designers a more complete understanding of the heat transfer and flow associated with film cooling of a turbine blade. In the end, this work, combined with others' work investigating how different factors influence film cooling, should allow engines to be run hotter and more efficiently. This would have far-reaching effects, impacting gas-turbine engines that are used in many different applications.

15. SUBJECT TERMS
Gas turbine, Film Cooling, Pressure Gradient

16. SECURITY CLASSIFICATION OF:			**17. LIMITATION OF ABSTRACT**	**18. NUMBER OF PAGES**	**19a. NAME OF RESPONSIBLE PERSON**
a. REPORT	**b. ABSTRACT**	**c. THIS PAGE**		51	**19b. TELEPHONE NUMBER** *(include area code)*

Standard Form 298 (Rev. 8-98)
Prescribed by ANSI Std. Z39.18

U.S.N.A – Trident Scholar project report, no. 499 (2020)

THE EFFECTS OF ACCELERATION ON FILM COOLING IN GAS TURBINE ENGINES

by

MIDN 1/C Clayton S. Pelzer
United States Naval Academy
Annapolis, Maryland

Certification of Advisers Approval

Professor Ralph J. Volino
Mechanical Engineering Department

_____

_____

Associate Professor Ronald Warzoha
Mechanical Engineering Department

_____

_____

Acceptance for the Trident Scholar Committee

Professor Maria J. Schroeder
Associate Director of Midshipman Research

_____

_____

USNA-1531-2

Acknowledgements

Thanks to Dan Rodgerson, Lou Becnel, and Steve Galindo for their wonderful support and hard work towards making this project a reality. Spending my 1/C year with them in the aero lab was a pleasure.

Thanks to Nick Hlavaty, Mike Superczynski, Brandon Stanley, and David Majerowicz for helping build the test section and wall.

Finally, thanks to my advisers for the massive amount of time and effort they have put into not only helping me along with the process, but for teaching me the extra material to help me understand the study itself.

Table of Contents

Abstract	1
List of Variables	2
Introduction	3
Methods	10
Results and Discussion	21
Conclusion	49
References	50

Abstract

Gas turbine engine blades contain film cooling holes that direct cool air over the surface of the blades, protecting them from high temperatures up to 2000 °C inside the turbines. There are many factors that affect film cooling, but one of the most important is the acceleration of flow over the surface of the blade. Its impacts on the film cooling process are not fully understood. Previous experiments have compared film cooling both with and without accelerating flow, but no study has reported on heat transfer and flow with different levels of acceleration. In order to understand the direct effects of acceleration, a test section was constructed to model the interactions of flow over a gas turbine blade by matching dimensionless parameters. The test section has lower temperatures and larger dimensions than an actual turbine blade, physically allowing for direct observation. The values determined through this work should give blade designers a more complete understanding of the heat transfer and flow associated with film cooling of a turbine blade. In the end, this work, combined with others' work investigating how different factors influence film cooling, should allow engines to be run hotter and more efficiently. This would have far-reaching effects, impacting gas-turbine engines that are used in many different applications.

Keywords:

Gas-turbine

Film Cooling

Pressure Gradient

List of Variables

B	Blowing Ratio
C_p	Pressure Coefficient
c_p	Specific Heat
D	Diameter of Test Wall Holes
h	Heat Transfer Coefficient
K	Acceleration Parameter
k	Thermal Conductivity
P	Local Pressure
P_i	Static Pressure at Inlet
P_T	Total Pressure
q''	Heat Flux
Re	Reynolds Number
St	Stanton Number
T	Local Temperature
T_{aw}	Adiabatic Wall Temperature
T_{jet}	Jet Temperature
T_∞	Mainflow Temperature
$U_{\infty i}$	Velocity of Flow at Inlet
W	Engine Total Work Output
η_{th}	Engine Thermal Efficiency
$\rho_{\infty i}$	Density of Flow at Inlet
θ	Dimensionless Temperature
ν	Kinematic Viscosity

Introduction

Gas turbine engines are widely used and come in many forms, from aircraft engines to stationary power generators. Clearly, increases in engine efficiency would be beneficial to a large audience, from airliner manufacturers to the Naval Surface Warfare community.

There are multiple ways to increase the efficiency of a gas turbine engine. Thermal efficiency is a measure of how much of the energy in the fuel is used to produce work. Equation 1 shows this definition, where η_{th} is thermal efficiency, W is total work output, and Q is the heat input [1]. The more efficient an engine, the more power output for the same amount of fuel.

$$\eta_{th} = \frac{W}{Q} \tag{1}$$

Gas turbine engines work by compressing air in a compressor, adding heat in a combustor, and removing energy with a turbine. Figure 1 below shows a simplified diagram of a gas turbine engine.

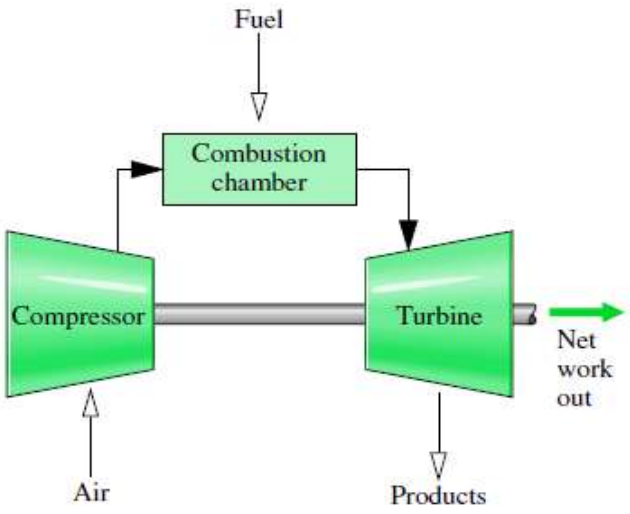

Figure 1 – A simplified gas turbine engine [1]

Increasing the pressure supplied by the compressor can lead to greater thermal efficiency. The hotter the mixture burns in the combustion chamber, the more thermally efficient the engine will be. Figure 2 shows how efficiency improves as temperature increases [2]. As a result of this relationship, engines today are designed to sustain extremely high temperatures in the turbine, in order to maximize efficiency. In fact, the temperature of the gas flowing around the blades is actually hotter than the melting temperature of the metal comprising the blades, which varies between 1260 °C and 1370 °C [3].

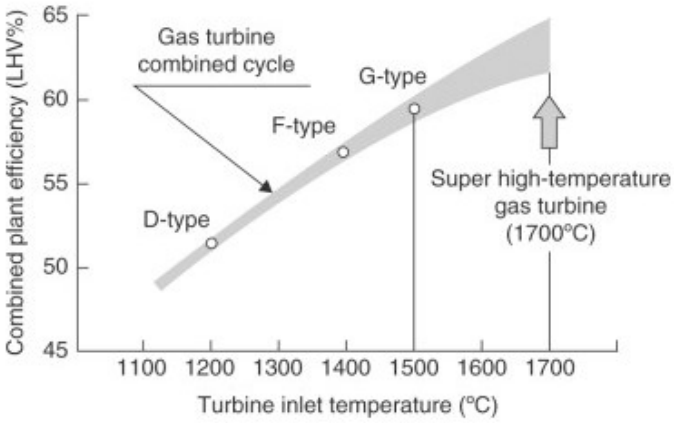

Figure 2 – Gas Turbine Plant Efficiency as a Function of Turbine Inlet Temperature [2]

The high temperatures and large acceleration forces experienced by the blades can cause thermal creep, which is very slow deformation induced by a force below the yield point of a material at high temperatures. Turbines rotate at high speeds, causing a longitudinal force along the blade in the radial direction. At high temperatures, the deformation resulting from this force can cause damage in modern engines, which are designed with very small clearance distances between the spinning blades and the outer casing of the turbine. Multiple strategies can be employed simultaneously to counter engine damage. These include the use of heat-resistant alloys, fabrication of blades from single crystals, covering the blades with ceramic thermal barrier coating,

and use of advanced cooling methods. The advanced cooling methods reroute relatively cool air from the compressor into the turbine blades themselves [2]. Figure 3 shows the design of a typical turbine blade with its cooling structures. The air is routed through internal cavities in the blade itself or out of film cooling holes along the surface of the turbine blade. The present work focuses exclusively on film cooling.

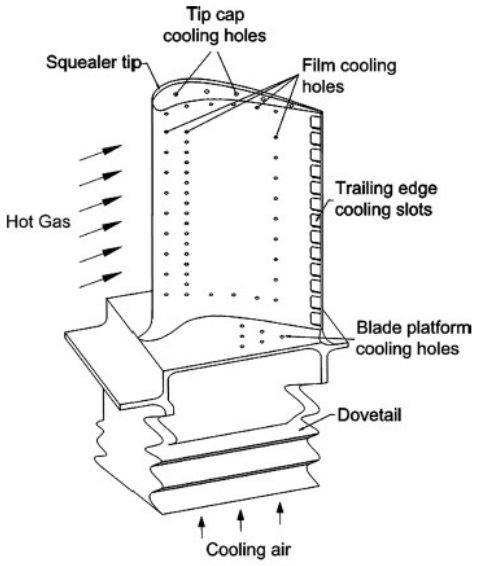

Figure 3– Turbine blade design and cooling structure [3]

Air from the film cooling holes is used to cover the turbine blades with an insulating layer or film of cool air. There are some energy losses associated with film cooling, caused by the loss of compressed air and disruption of flow. The air used for film cooling is part of the bleed air that is rerouted from the compressor, taking away air that would otherwise be used in the cycle. In fact, in high-performance turbines, approximately 20-25% of the compressed air is used for cooling [2]. Since the bleed air used for film cooling does not produce work, it introduces some loss into the system. Additionally, any disruption of flow over the surface of the blades can increase aerodynamic or total pressure losses. Overall, however, the ability to raise the combustion to higher temperatures more than offsets the losses introduced by film cooling.

The flow of the hot gas over the blade has a large influence on how well film cooling works. Acceleration of air around wing-shaped airfoils is a key element of lift production. Changes in pressure are introduced due to the airfoil shape, shown in Figure 4, where pressure coefficients are shown for a specific blade shape.

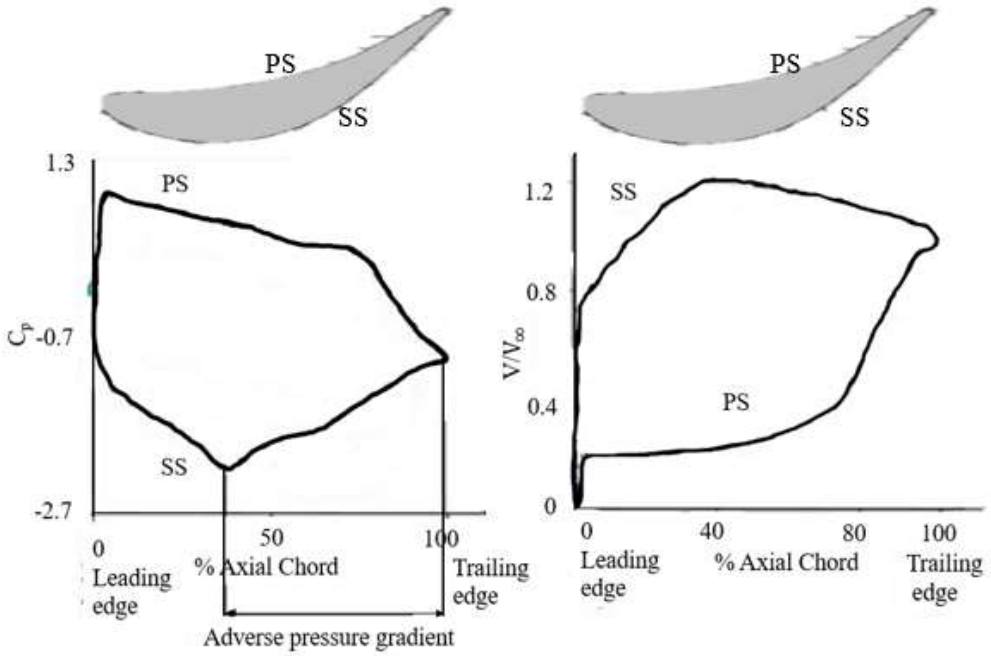

Figure 4 – Pressure and velocity distribution on blade surface at different spanwise locations. Adapted from [4].

The pressure coefficient is defined as the difference between local pressure and a reference pressure, divided by dynamic pressure (pressure due to kinetic energy of fluid particles). C_p is a common parameter given for various airfoils, relating pressure along the surface of an airfoil to the surrounding pressure [5]. The standard definition of C_p is given in Equation 1. P_T is the total pressure, P_i is static pressure at the inlet, and P is local pressure along the airfoil. $U_{\infty i}$ is the inlet freestream (mainflow) velocity, where $\rho_{\infty i}$ is the density of the flow at the inlet.

$$C_p = \frac{P - P_i}{\frac{1}{2}\rho_{\infty i} U_{\infty i}^2} = \frac{P - P_i}{P_T - P_i} \tag{1}$$

Bernoulli's equation (Equation 2), shows that these two versions of C_p are equal. Total pressure is equal to the combination of static and dynamic pressure.

$$\boldsymbol{P_T = P_i + \frac{1}{2}\rho_{\infty i} U_{\infty i}^2} \tag{2}$$

Using C_p values determined experimentally for specific turbine blades in conjunction with Bernoulli's equation and the inlet velocity of the fluid, the freestream velocity along the blades can be calculated. Figure 4 shows the typical distribution of C_p and velocity along a blade. The pressure side (PS) experiences a favorable pressure gradient (decreasing pressure, increasing velocity) along nearly its entire surface, while the suction side (SS) experiences a favorable pressure gradient, followed by an adverse pressure gradient towards its trailing edge.

Only a few studies have looked directly at acceleration effects on film cooling. Vinton et al. [6] looked at how a favorable pressure gradient (acceleration of flow) impacted the film cooling effectiveness. The work compared one favorable pressure gradient to a zero pressure gradient (no acceleration) and showed that a pressure gradient did not change the effectiveness on average, but did change which areas were affected by the film cooling along the test plate. The reason for this change could not be fully explained.

Lutum et al. [7] studied film cooling effectiveness and heat transfer coefficients over a concave surface with a favorable pressure gradient. This study examined 5 different injection configurations and calculated values for film cooling effectiveness and heat transfer coefficients. The work found that film cooling effectiveness was increased with an accelerating flow near the hole, while farther downstream, the test wall film cooling performance decreased. There was little effect on the heat transfer coefficients, but overall, film cooling effectiveness decreased due to the freestream acceleration.

Coletti et al. [8] utilized magnetic resonance imaging (MRI) to investigate the impacts of favorable and adverse pressure gradients on the flow from a single cooling hole, documenting full 3D velocity fields on flat and curved test plates. The work found that an acceleration of flow causes a thinner boundary layer thickness. The boundary layer is the layer of fluid along a surface where the velocity is lower than the freestream velocity, due to the effect of fluid friction along the surface. Additionally, they found that configurations with weak wall curvature such as the surface of a turbine blade can be well represented by flat plate experiments. However, the study did not take direct cooling efficiency or heat transfer measurements.

Maiteh and Jubran [9] studied the effects of one specific favorable and one adverse pressure gradient, and how they affected the film cooling effectiveness for different hole types and orientations. The work found that offsetting film cooling holes instead of putting them inline made film cooling effectiveness higher. Additionally, the presence of favorable pressure gradients led to dilution of injected coolant jets, reducing film cooling protection over the surface. An adverse pressure gradient appeared to dilute the coolant even more than the favorable pressure gradient. The study did not measure the flow over the surface of the test wall.

Schmidt and Bogard [10] looked at one pressure gradient distribution and compared it to a similar case with a zero pressure gradient. They found that accelerating flow led to a wider spread of the film cooling jet near the hole. The acceleration rate was small however, and the boundary layer was thin enough that it was expected to have limited influence on results. They found that acceleration increases shear, which in turn increases the rate at which jets are mixed with the freestream flow.

The previous experiments all investigated accelerating flow to some extent, but none of them studied multiple levels of acceleration. Many of them also observed how hole shape and curvature

of the test wall influence film cooling rather than focusing only on acceleration. Many of the results are contradictory with regards to the effect on the flow, and research into the direct effects of acceleration on film cooling has been limited. This study provides documentation of the flow and heat transfer in film cooling flows with varying levels of acceleration. The information gathered may be used to improve gas-turbine cooling so that engines can run more efficiently.

Methods

Once velocities in a main flow are determined, they can be utilized to calculate the acceleration parameter *K*, which is defined in Equation 3, where the kinematic viscosity is given as *v*. The value U_∞ is the local freestream velocity along the blade, and x is the streamwise coordinate along the blade surface. A positive acceleration parameter is synonymous with a favorable, negative pressure gradient; a negative acceleration parameter is the same as an adverse, positive pressure gradient.

$$\boldsymbol{K = \frac{v}{U_\infty^2}\frac{dU_\infty}{dx}} \tag{3}$$

In order to investigate the effects of accelerating flow on cooling jets, a model based on the inside of a gas turbine was developed. Naturally, it would be exceedingly difficult to precisely match all of the parameters of real turbine flow, given the very high temperatures, rotating environment, and small size. Even if values could be measured, many different factors would be affecting results, rendering explanation extremely difficult. By matching dimensionless parameters, a simplified but useful representation of the flow inside an actual gas turbine engine can be produced. Essentially, the model will use dimensionless numbers to create a scenario that can be maintained in a laboratory environment. As a result, hot air will be blown from jets into a cool mainstream flow to determine the effects of acceleration. In this case, the hot and cold temperatures are reversed as compared to a real engine, but this does not impact the dimensionless results because only the temperature difference matters.

Governing physical laws are obeyed in all flow situations, and these laws can be represented with equations. In principle, the equations can be used to solve for temperature and heat transfer values for a surface. However, solving the equations analytically for a film cooling scenario is impossible,

and solving them numerically would be a computationally expensive task. Instead, this study will address the problem experimentally, using a laboratory model. The model will be representative of a turbine flow if geometric and dynamic similarity are achieved between the model and the turbine. Dynamic similarity is achieved by matching dimensionless parameters. Matching some non-dimensional quantities between two scenarios results in other quantities being matched. For this study, matching the Reynolds number, Prandtl number and blowing ratio will cause the values of the film cooling effectiveness and Stanton number in the experiment to match numbers in an actual engine.

Reynolds number (Re) is defined in Equation 4, based on U_∞, the diameter of the film cooling hole, D, and the kinematic viscosity, ν. The value of $U_\infty$and D will be chosen so that the Re will be roughly 10,000, which is representative of the value in a turbine. All of the material properties in the parameters are for the fluid.

$$\boldsymbol{Re} = \frac{\boldsymbol{U_\infty D}}{\boldsymbol{\nu}} \tag{4}$$

Additionally, the Prandtl number (Pr) will be matched in order to establish similitude in heat transfer and film cooling effectiveness. The definition of Pr is shown in Equation 5, where c_p is specific heat, μ is dynamic viscosity, and k is thermal conductivity. The Prandtl number for the experiment will be 0.7, while in a real engine it will be roughly 0.74. The proximity of these values suggests that the experiment will be representative of a turbine.

$$\mathbf{Pr} = \frac{\boldsymbol{c_p \mu}}{\boldsymbol{k}} \tag{5}$$

The blowing ratio, B, is defined in Equation 6. In the tests that were conducted, the density of the air in the jet (ρ_{jet}) will be within 1% of the density of the air in the main flow (ρ_∞) because they will differ by only a few degrees in temperature. The blowing ratio is therefore approximately

equal to the velocity ratio V_{jet}/U_{∞}. V_{jet} is the air velocity flowing out of the cooling hole. Figure 5 shows the effects of increasing the blowing ratio on a cross-sectional view of dimensionless flow temperature values. The planes in the diagram are perpendicular to the main flow, and the bottom of the plots are along the blade surface. The planes are 7 hole diameters downstream of the film cooling hole. The contours show the dimensionless temperature, which is defined in Equation 7.

$$\boldsymbol{B = \frac{\rho_{jet} V_{jet}}{\rho_{\infty} U_{\infty}}} \tag{6}$$

The dimensionless main flow temperature is 0, while temperature of the air leaving the hole is 1. On the left side, blowing ratio is 0.5; on the right it is 1. A higher blowing ratio can lead to liftoff, where the airstream from the jet lifts off of the surface. This liftoff is detrimental because less cooling air is interacting with the surface of the blade, decreasing the blade cooling.

$$\boldsymbol{\theta = \frac{T - T_{\infty}}{T_{jet} - T_{\infty}}} \tag{7}$$

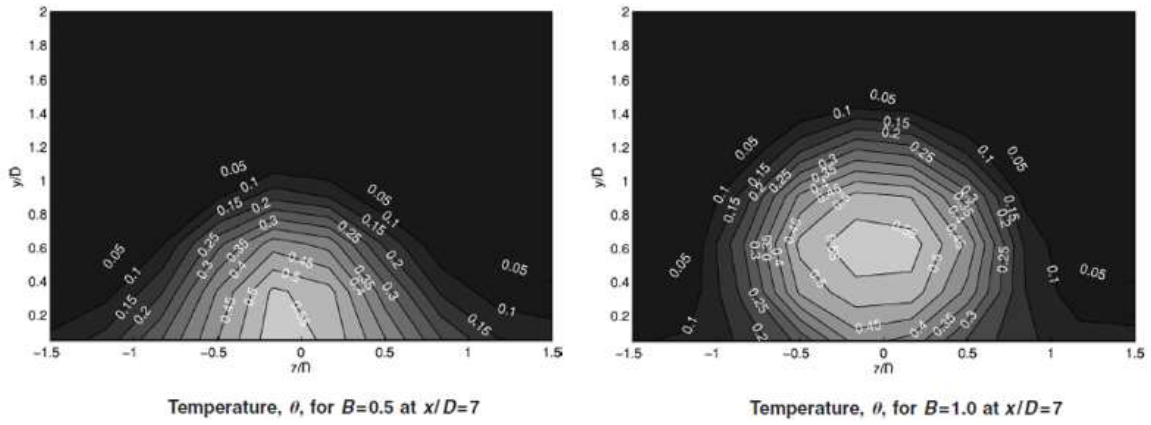

Figure 5 - Effects of blowing ratio on temperature distribution [14]

If Re, Pr, and B are matched between the engine and laboratory environment, then the film cooling effectiveness and dimensionless heat transfer coefficients will also match. Film cooling effectiveness is one of the best ways to quantify the effectiveness of the cooling jet at various

points around the film cooling holes. The effectiveness is represented by η, which is defined using Equation 8. T_{aw} is the temperature of the test wall if it were adiabatic (zero heat transfer), T_∞ is the temperature of the main flow, and T_{jet} is the temperature of the air flowing out of the cooling jet.

$$\boldsymbol{\eta = \frac{T_{aw} - T_\infty}{T_{jet} - T_\infty}} \tag{8}$$

The Stanton number (St), defined in Equation 9, is a dimensionless parameter representing a form of the heat transfer coefficient.

$$\boldsymbol{St = \frac{h}{\rho c_p U_\infty}} \tag{9}$$

The value h is the heat transfer coefficient, usually determined experimentally since there are many factors that influence the coefficient. As a result, it is nearly impossible to determine analytically except in the simplest cases. In Equation 10, the heat flux, q", is the heat transfer per unit area. T_s is the temperature of the test wall when it is non-adiabatic.

$$\boldsymbol{q'' = h(T_s - T_{aw})} \tag{10}$$

The heat transfer rate and temperatures were measured in the experiment and used to determine η and St. The same η and St can be applied to engine conditions and used to determine the temperature and heat transfer for an actual turbine blade. In the case of turbine blade cooling, a high cooling effectiveness and a low St are desirable. If the cooling effectiveness is higher, the surface temperature is closer to T_{jet}, the cooling air temperature. If the cooling effectiveness is increased, the flow temperature T_∞ can be increased to make the engine more efficient overall. A low St means that less heat is transferred between the surface and flow. Because the surface temperature is lower than the main flow temperature, any heat flow will increase the surface temperature or increase the need for cooling inside the blade.

Three main quantities were measured in the model: air velocity (u), air temperature (T_{air}), and test wall temperature (T_{wall}). In order to measure u, a hot-wire probe was moved throughout the steady-state flow, measuring hundreds of points in a grid. A thermocouple probe was also moved through a grid and used to measure air temperature. In order to determine the temperature on the wall itself, an infrared (IR) camera was placed to measure temperatures through an IR window in front of the test wall.

Hot-wire anemometry (HWA) is a method used to measure flow velocity in fluid dynamics applications. A drawing of a typical probe is shown in Figure 6. It consists of two prongs with a wire stretched across them. An electric current is sent along the wire, producing resistance heating. Fluid flows over the wire, removing energy while the anemometer adjusts the supplied voltage to maintain a constant wire temperature. If the velocity increases, voltage is increased to counteract the cooling. Consequently, velocity can be determined from voltage [11]. Hot-wire probes are very small (microns thick) and sensitive (±0.1 m/s) to changes in velocity, giving them a high measurement resolution and making them a good option for this project. Velocity at multiple points in the flow were measured using HWA.

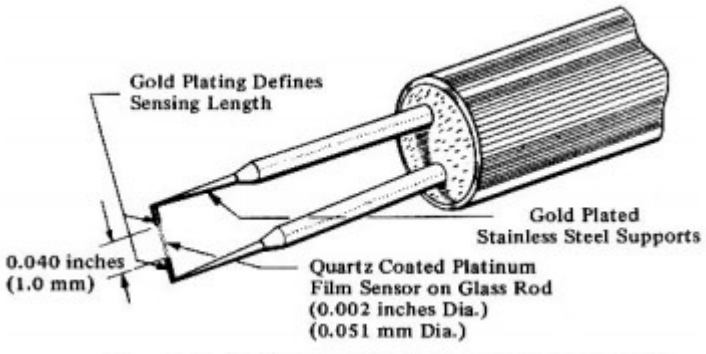

Figure 6 - Hot-wire probe [11]

Thermocouples were used to measure the temperatures in the flow, along with T_{jet} and T_∞. The thermocouples are made up of two wires of different metals that form electrical junctions. The thermoelectric effect produces voltage changes when temperature changes, allowing temperature to be measured [12].

In an actual gas turbine engine, the main flow is hot while the jets and internal blade flow are cooler. Thus, heat flows from the hot main flow into the cooler blade surface. For convenience in the experiment, it is simpler to heat the test wall than to cool it, so both the direction of heat transfer and the sign of the temperature difference between the main flow and jets were reversed. The main flow was cooler, the jets were warmer, and heat flowed from the test wall into the main flow. Based on Equation 8, the film cooling effectiveness remained the same value, as the signs of both the numerator and denominator were both reversed. Since both the signs of q" and the temperature difference in equation 10 remained the same, the heat transfer coefficient and Stanton number in Equation 9 were unaffected.

An infrared (IR) camera was used to measure the temperature everywhere on the test wall. Two trials were done for each case. T_{aw} was measured in the first scenario with the wall unheated, and T_s in the second with the wall heated with an electric surface heater. All materials emit infrared electromagnetic waves, depending on the surface temperature and emissivity. As temperature increases, intensity of the infrared waves increases. Thermographic cameras use microbolometers, which consist of two layers of plates. When waves hit the plates in individual pixels, electrical resistance is created. The imager's electronics then convert these resistances into thermal images and temperature values [13].

For all cases, measurements of the test wall temperature were made with the IR camera. For each case the temperature field was measured twice, once with the electric wall heaters on, and once

with them off. The freestream and jet temperatures were simultaneously measured for each case with thermocouples. After the measurements were completed for all cases, problems were discovered that affected the results.

The IR images with the heaters active showed unexpected hot and cold patches and streaks that indicated that the wall heat flux was not uniform. The non-uniformity was either due to non-uniformity in the heater itself, or more likely non-uniformity in the way the heaters were affixed to the Formica surface of the test wall. Attempts to estimate the local heat flux were made, but the non-uniformity was large, making it impossible to obtain a sufficiently accurate estimate to obtain any meaningful heat transfer coefficient or Stanton number results. These results, therefore, are not presented.

Film cooling effectiveness was obtained from the results obtained with the electric heaters inactive. These results showed expected trends, but also showed significant differences from results in the literature, as will be shown below. Subsequent to the measurements, the calibration of the instruments was checked. The IR camera readings were found to be accurate to within 0.5 °C, which is 3.5% of the jet to freestream temperature difference. The thermocouple readings were found to be highly inaccurate, with errors of 2 °C near the temperature of the measurements to as high as 13 °C when checked against an a 0 °C icepoint. The reason for the large uncertainty was not determined. The estimated uncertainty in the camera measurements is 0.8 °C for the range of interest of the measurements. The combined uncertainty from the camera and the thermocouple measurements results in a 56% uncertainty in the film cooling effectiveness results. Plans were made to repeat the measurements, but could not be completed within the time available for this project.

The measured data acquired using the instruments were used to compute the dimensionless parameters described above. Film cooling effectiveness was determined with the values T_{aw}, T_{jet}, and T_∞ from Equation 8. T_{aw} was measured everywhere on the test wall with the IR camera, while T_{jet} and T_∞ were determined from thermocouples. Figure 7 shows an example from Coulthard et al. [14] which is characteristic of the film cooling effectiveness results that were calculated.

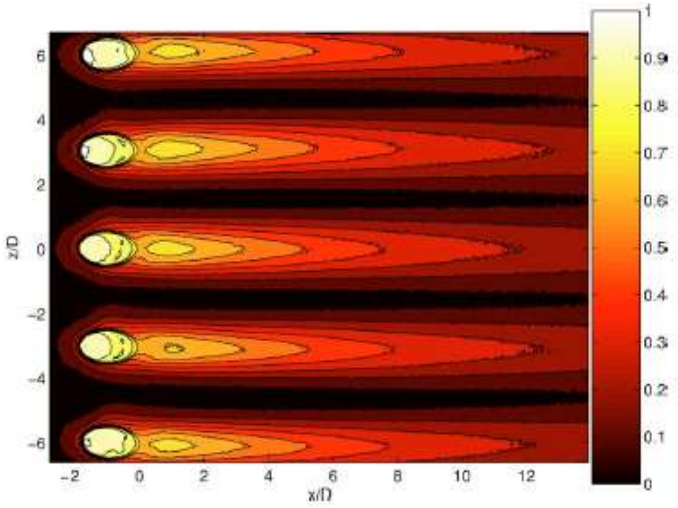

Figure 7 – Film cooling effectiveness contour plot [14]

The Stanton number (St) was calculated from the known value q″, based on the voltage and electrical resistance of the wall heater. Then, using the values T_{aw} and T_s determined from the IR measurements in the unheated and heated cases, h was calculated. Once h was found, St was calculated from Equation 9. As noted above, the Stanton number results will not be presented.

Table 1 shows the experimental matrix. At four different levels of acceleration, four different blowing ratios were evaluated.

Table 1-Project Experimental Matrix

Case Number	Acceleration Parameter	Blowing Ratio
1-4	0	0, 0.5, 1, 1.5
5-8	$5x10^{-7}$	0, 0.5, 1, 1.5
9-12	$1x10^{-6}$	0, 0.5, 1, 1.5
13-16	$5x10^{-6}$	0, 0.5, 1, 1.5

The testing apparatus set up was very similar to that used in Coulthard et al. [14]. Figure 8 shows the set-up for the open-loop subsonic wind tunnel that was used to establish flow of air at 0.47 m^3/s over the test wall. The heat exchanger, honeycomb, and screens all served to maintain uniform velocity and temperature in the flow of air. A blower was connected to the diffuser, providing a steady stream of air through the entire configuration. The motor used to provide air flow uses 220V 3-phase power, so a variable frequency drive was used to adjust the frequency of the power. Changing the frequency changes the rotations per minute (rpm) of the blower, varying the flow rate. The fan pushed air through the tunnel while a chilled heat exchanger maintained a uniform, cool main flow.

The test section was attached at the exit of the nozzle, and is shown in Figure 9. The test section consisted of the test wall with the film cooling holes, an opposite wall and end walls to guide the air flow, and a plenum to supply the film cooling air. The film cooling air entered the plenum from a manifold that was supplied with a high-pressure source of air. The plenum can be seen on the back of the test section in Figure 9. An orifice plate between the manifold and the plenum was used to meter the air flow into the plenum, and the flow rate was controlled with a pressure

regulator on the supply to the manifold. A heat exchanger in the plenum maintained the jet temperature by using heated water flow, transferring heat to the air in the jets.

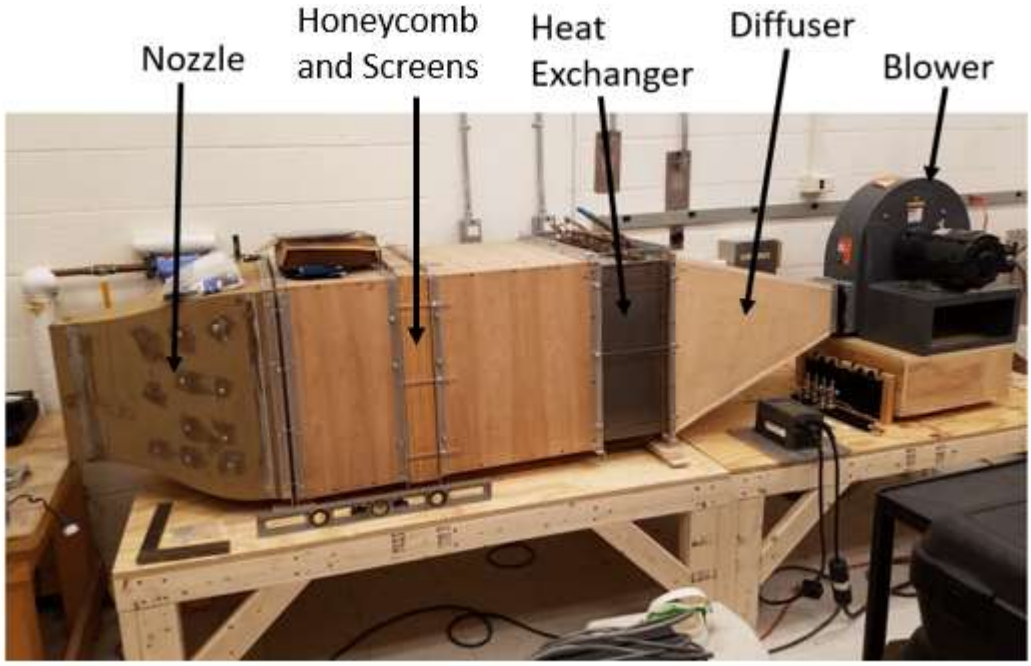

Figure 8 – Wind tunnel configuration

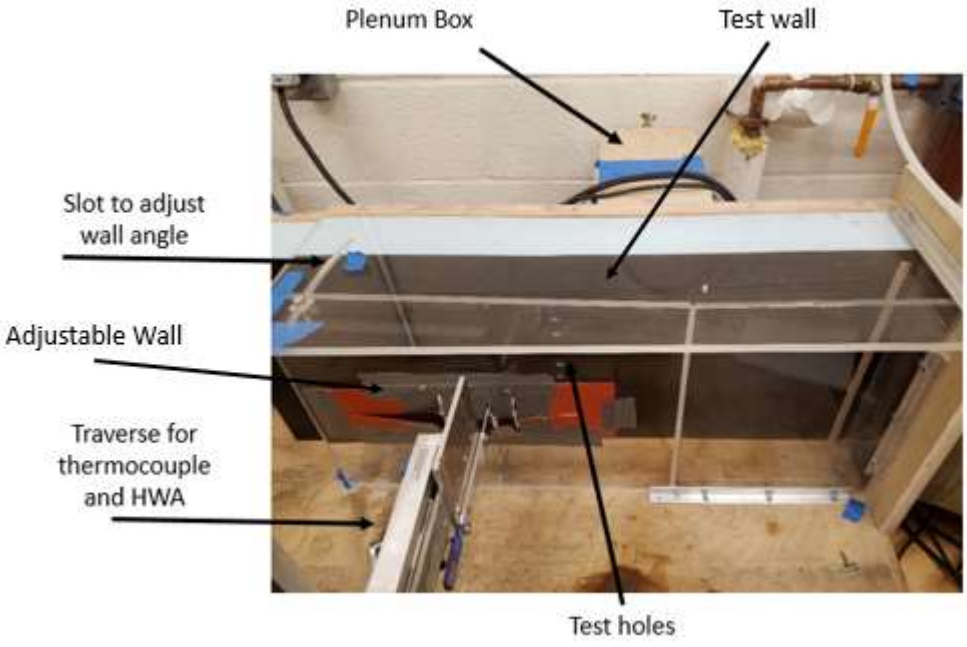

Figure 9 – Completed Test Section Build

The test wall with film cooling holes was designed to test temperatures and flow. The wall was made of extruded polystyrene (Styrofoam) and had 9 cooling holes. Each of the holes was oriented at an angle of 35° to the surface, a standard value for film cooling tests [14]. Each hole had a diameter of 9.525 mm, which is much larger than actual film cooling holes in turbine blades.

A side-view of the test wall is shown in Figure 10. The test wall consisted of a wood frame, a 101.6 mm thick layer of Styrofoam, two thin heaters, and a thin layer of Formica on the front surface. The Styrofoam insulated the back side of the wall so that the heat from the heaters went through the Formica rather than escaping into the air on the back surface.

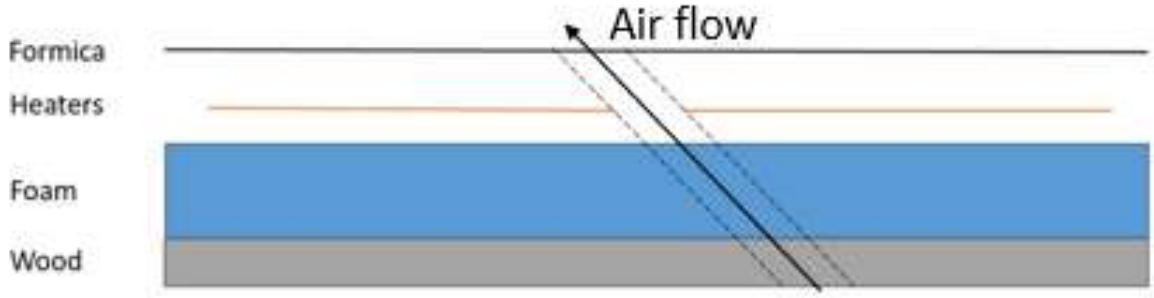

Figure 10 – Layering of Test Wall

Because the main investigated topic in this study was the effects of accelerating flow (a favorable pressure gradient) the test chamber had an adjustable cross-sectional area. In order to induce steady acceleration across the test wall, the freestream velocity was set using a nozzle-type structure. When the air flow passed through the test chamber, the decreasing cross-sectional area forced the air to accelerate spatially. The adjustable wall in Figure 9 was moved to set the rate of acceleration. There were two versions of the adjustable wall. For one, an IR window was placed in the adjustable wall so that an IR camera could make direct measurements through the window to the test wall. The other wall had slots for the insertion of probes to measure velocity and temperature.

Results and Discussion

To compare results, a coordinate system was defined, as shown in Figure 11 below. The x-direction is in the same direction as the freestream velocity. The z-direction is in the spanwise direction, parallel to the test wall and perpendicular to the freestream flow. The Y-direction is the distance off the test wall. The origin of the coordinate system is on the test wall at the downstream edge of a hole, shown in Figure 11.

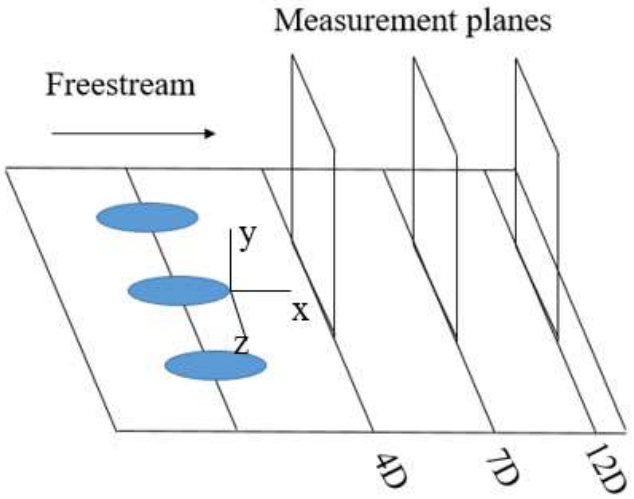

Figure 11 – Coordinate System for Test Wall

In order to determine settings for the blowing ratio, the velocity of the air coming out of the hole was determined. To do this, the hot wire anemometer was used to measure velocity at points in a two dimensional grid at the hole exit plane, with a specific set pressure provided to the plenum. The measurement points in the plane formed a grid with 2 mm spacing in the x and z directions. Figure 12 shows a contour plot of the velocity coming out of the hole. The red line shows the outline of the hole. As expected, the center of the holes has a higher velocity than the sides. The jets flowing through the holes in the test wall behaved as flow through a pipe, and the boundary layer on the sides of the pipe causes the velocity to decrease near the pipe wall.

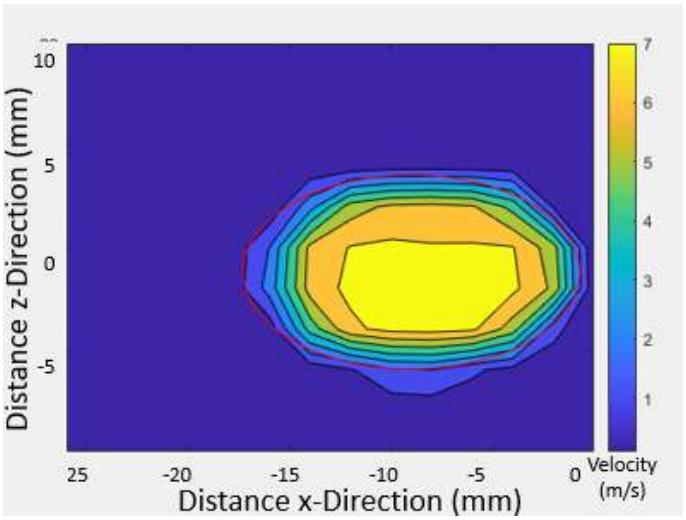

Figure 12 – Velocity Contour Plot Over Holes

In order to address the non-uniform flow from the holes, a line of velocity and turbulence measurements was taken in the streamwise direction over the spanwise centerline (z=0) of the holes for each blowing ratio. An example of one of these measurements can be seen in Figure 13, typifying the shape of the velocity distribution. At each measurement location, velocity data were acquired for 26 seconds at a 20 kHz sampling rate. The time averaged velocity distribution is shown on the left in Figure 13. The velocity is not perfectly steady due to turbulent fluctuations, and the turbulence is defined as the root mean square of the fluctuating velocity. The turbulence distribution is shown on the right in Figure 13. Moving from the leading edge of the holes to the trailing edge, the velocity increases sharply, plateauing at the center of the hole. Note that in the plane of the test wall, the projection of the round hole is an ellipse of length D/sin(35°) = 16.6 mm. The small changes that can be seen at the top of the velocity plot are most likely due to the pressure in the line slowly oscillating as the compressor providing the building compressed air turns on and off. The turbulence is highest near the edges of the jet, where a shear layer is formed between the jet fluid and the air outside the jet. The effect of this will be shown later in the velocity profiles measured in the main flow. The turbulence decreases near the center of the jet hole.

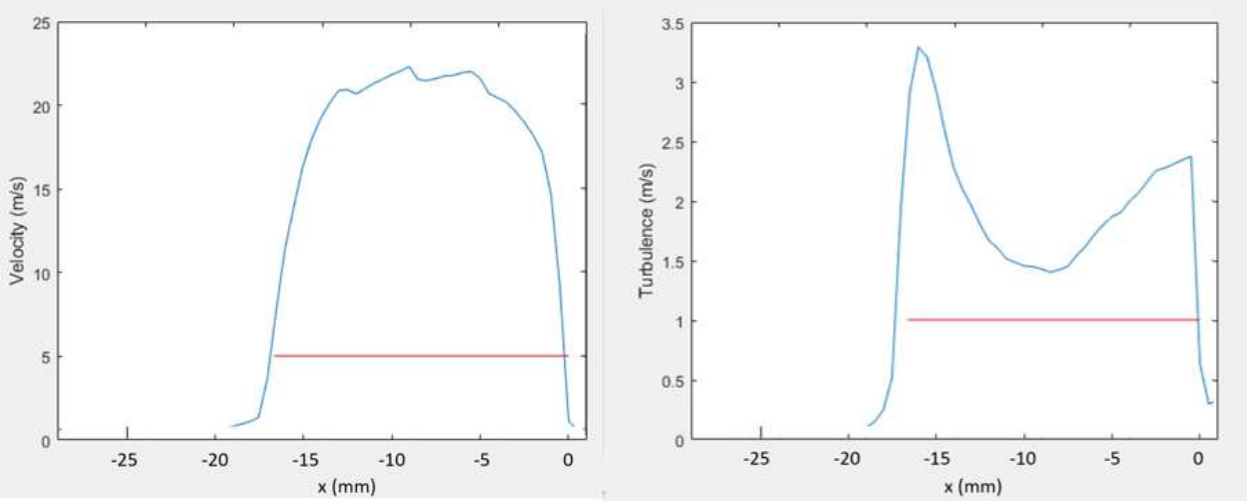

Figure 13 – Velocity and Turbulent Measurements Across the Centerline of Plenum Holes. The Red Horizontal Line Indicates the Location of the Hole

The designed plenum was unable to produce the velocity required for each blowing ratio with all 9 holes in the test wall. As a result, holes were covered with thin tape to increase the flow through the remaining open holes.

The values of the velocities across the hole were integrated and averaged to find the bulk velocity of the jet. Table 2 shows the bulk velocities desired and the ratio between the bulk velocity and maximum velocity at the center of the holes. For each blowing ratio, the upstream pressure in the manifold supplying the plenum was determined and the temperature of the jet air was measured.

Table 2 – Characteristics of Jet at Each Blowing Ratio

Nominal blowing ratio	Hole Center Velocity (m/s)	Bulk Velocity (m/s)	Number of holes open	Required Max Pressure (psi)	Jet temperature (°C)
0.5	8.5	5.3	5	29	33.5
1	15.2	10.64	4	68	32.2
1.5	18.1	12.85	3	75	31.6

Once the values for the individual blowing ratios were computed, the temperature and velocity uniformity of the wind tunnel was determined at the inlet plane of the test section, which is also the exit plane of the nozzle. The temperature distribution can be seen in Figure 14. The probe was traversed through a grid in the plane with 5 mm spacing in the x and y directions. The temperature throughout the entire cross-section was uniform to within 0.5 °C. The left side of the graph shows the flow closest to the test wall. The far wall of the test section is warmer than the flow closest to the test wall due to the higher temperature of the surroundings outside of the test section. The test wall is insulated with Styrofoam. The area extending from the test wall to y = 50 mm is where measurements were taken. The temperatures in this region remained remain relatively constant between 20.4 and 20.65 °C. Thus, the temperature was assumed to be essentially constant in the main flow for this experiment.

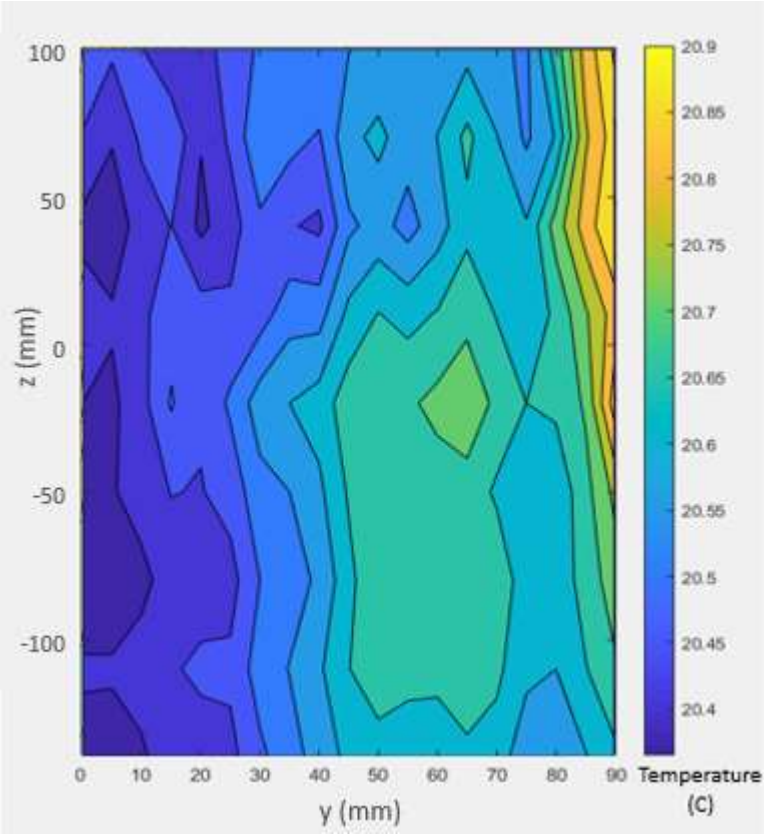

Figure 14 – Temperature Profile of Test Section Inlet

Figure 15 shows a velocity grid in the same plane at the exit of the nozzle. The velocity of the main flow remains very nearly constant at 12 m/s. The boundary layer can be seen on the walls around the test section, where the velocities are lower. Outside of the boundary layers, the velocity is uniform out to y = 50mm. This indicates that assuming a constant freestream velocity for the inlet of the test section is reasonable, since measurements will only be taken out to this distance. In general, the wind tunnel successfully brought the main flow to a constant, steady temperature and velocity.

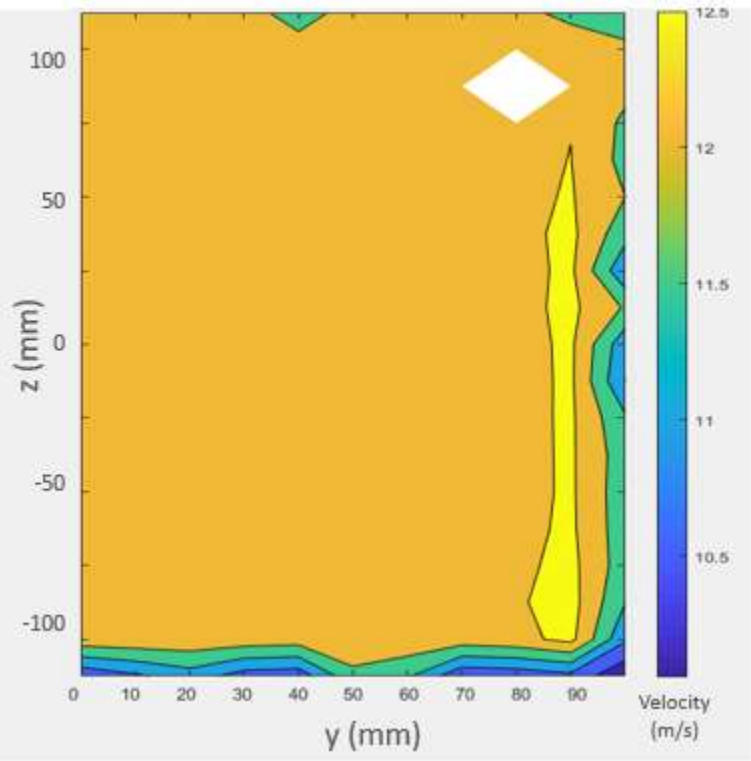

Figure 15 – Velocity Profile at Wind Tunnel Outlet

In addition to the velocity and temperature measurements at the test section inlet, a velocity profile was taken to determine the boundary layer thickness without jets or acceleration, at a point 0.5 D upstream of the hole. This baseline boundary layer can be seen below in Figure 16. The boundary layer reflects what is expected. The dimensionless values of u^+ and y^+ follow closely the "Law of the Wall," represented by the pink and green lines on Figure 16. Equation 11 shows the definition

of y^+ and u^+ below. A trip installed at the leading edge of the test wall induced a turbulent boundary layer that behaves as expected. Once all of these tests on the test section and wind tunnel were performed to verify expectations, the test cases were begun.

$$y^+ = \frac{yu_\tau}{\nu}, u^+ = \frac{u}{u_\tau} \tag{11}$$

y = Distance in y direction

u_τ =Friction velocity

u = Flow velocity

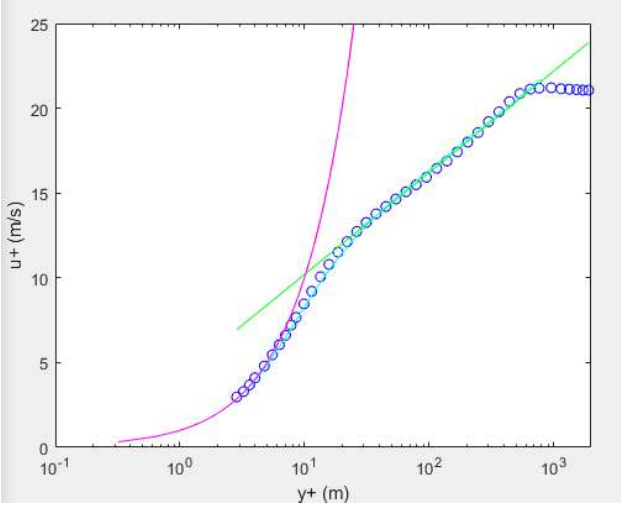

Figure 16 – Velocity Profile 0.5D Upstream of Holes, K = 0,B= 0

For each of the cases in Table 1, the acceleration parameter was determined by measuring the freestream velocity at multiple points separated by a known distance, and the angle of the wall opposite the test wall was adjusted to produce the desired K value. The angle between the test wall and opposite wall and blower motor RPM required were recorded for each K.

Flowfield Temperature and Velocity Measurements

Figure 11 shows the placement of three temperature measurement planes taken for each case. These measurements were taken in the flow in a y-z plane at x = 4D, 7D, and 12D downstream of the holes. Measurements were acquired in each plane in a grid with 1 mm spacing in the y and z directions. The planes were centered on the middle hole in the test wall.

An example temperature grid from the main flow can be seen below in Figure 17. The temperature grids were symmetrical, allowing only half of the grid to be plotted to visualize the entire jet. To compare cases with and without acceleration, the temperature grids were merged together for each blowing ratio and position, with results for K=0 on the left and K > 0 on the right. The jet can be clearly seen in the center of the plot, which displays θ as a function of dimensionless distance from the hole along the z and y axes. The shape of the jet is clearly visible, with higher temperature in the middle of the jet and a temperature gradient on the outside of the jet. The presence of the test plate can be seen where the jet "widens" at the bottom of the plot, as part of the jet sits along the plate.

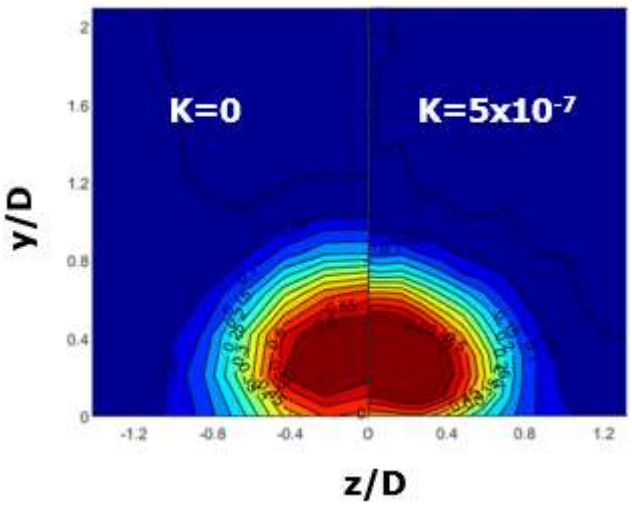

Figure 17 – Example of Temperature Grid, with Dimensionless Temperature as a Function of Distance from Hole in the Z and Y Directions

Figure 18 shows the temperature grids at various positions and blowing ratios throughout the flow. The distance from the holes increases moving from left to right – 4D, 7D, and 12D away from the hole respectively. The blowing ratio increases moving from top to bottom- 0.5, 1, and 1.5 respectively. These figures are all on the same dimensionless position and temperature scales.

As distance from the holes increases, the jet decreases in average temperature, as more heat is transferred between the jet and the main flow. The jet begins to spread out as it moves through the flow as well, which is apparent from the increased liftoff as the jet moves down the plate. This behavior is expected for the jet. As blowing ratio increases, the liftoff of the jet also increases. Since the jet is angled at 35° to the surface, it has a velocity component in the y direction, pushing it off of the surface of the test wall. Double vortices can be seen as blowing ratio increases, most clearly in Figure 18g with the highest blowing ratio at the closest position to the hole. Figure 18g shows these vortices and their relative motion, observable from the curved nature of the high temperature jet center.

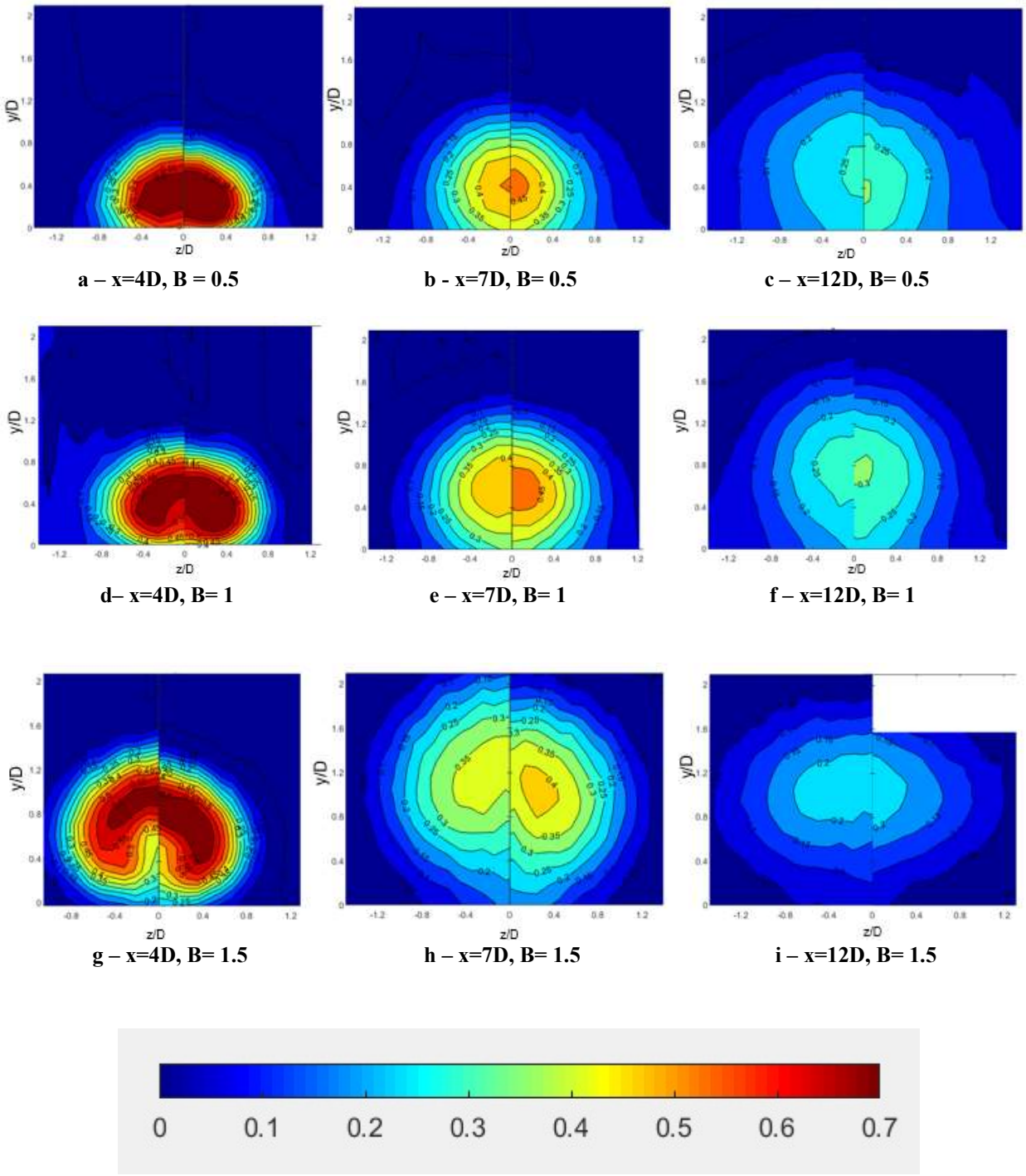

a – x=4D, B = 0.5 **b - x=7D, B= 0.5** **c – x=12D, B= 0.5**

d– x=4D, B= 1 **e – x=7D, B= 1** **f – x=12D, B= 1**

g – x=4D, B= 1.5 **h – x=7D, B= 1.5** **i – x=12D, B= 1.5**

Figure 18 – Temperature of jets at various x distances and blowing ratios

Acceleration of the main flow appears to have a few effects on the shape and position of the jet. In all of the temperature plots, acceleration decreases the amount of liftoff for the jet: all of these jets

are closer to the test wall. The liftoff is more apparent at higher blowing ratios, with a difference in the position of the outer shear layer of the jet which is about 0.2D closer to the wall in the case with acceleration. The difference between amounts of liftoff can be partly explained with velocity profiles, which follow this discussion of temperature grids. Additionally, the acceleration causes a higher average temperature in the jet, most clearly seen at x = 7D. The higher average most likely results from the decreased turbulence that acceleration causes.

In order to investigate the temperature profiles of the jets further, a single line profile was taken from the temperature grids at z/D = 0. These profiles can be seen in Figures 19 through 21. Dimensionless temperature is shown as a function of dimensionless distance in the y-direction. The cases without acceleration are indicated with solid lines, while the cases with acceleration are denoted by dashed lines.

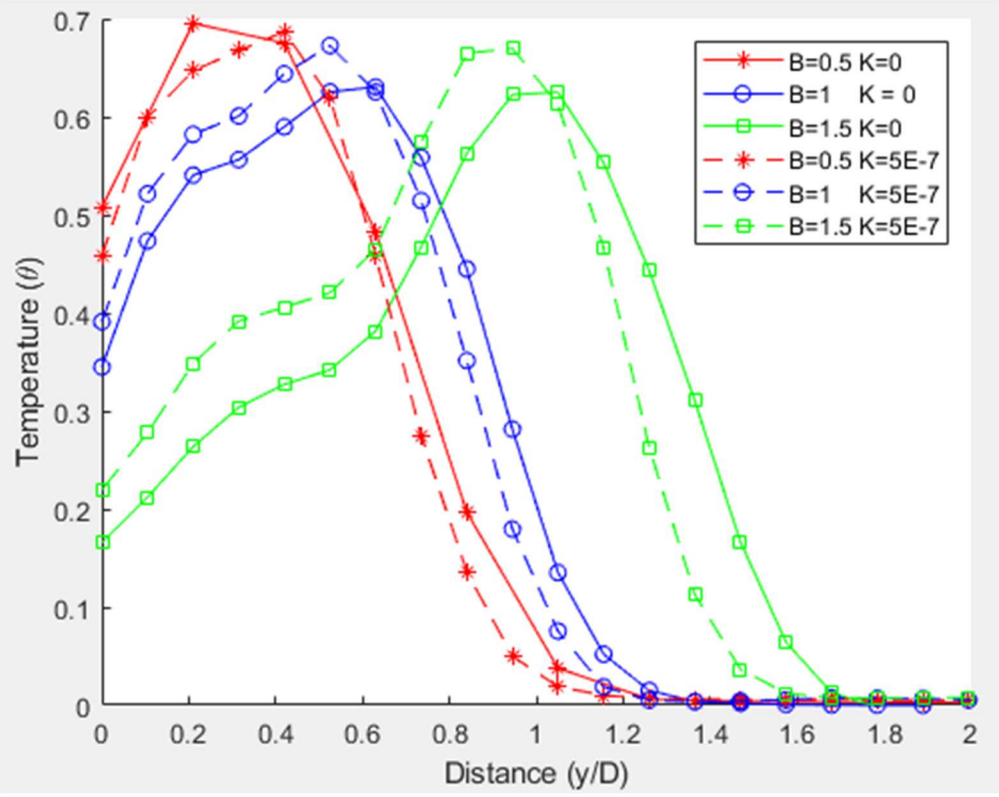

Figure 19 – Temperature Profiles Z=0, X=4D

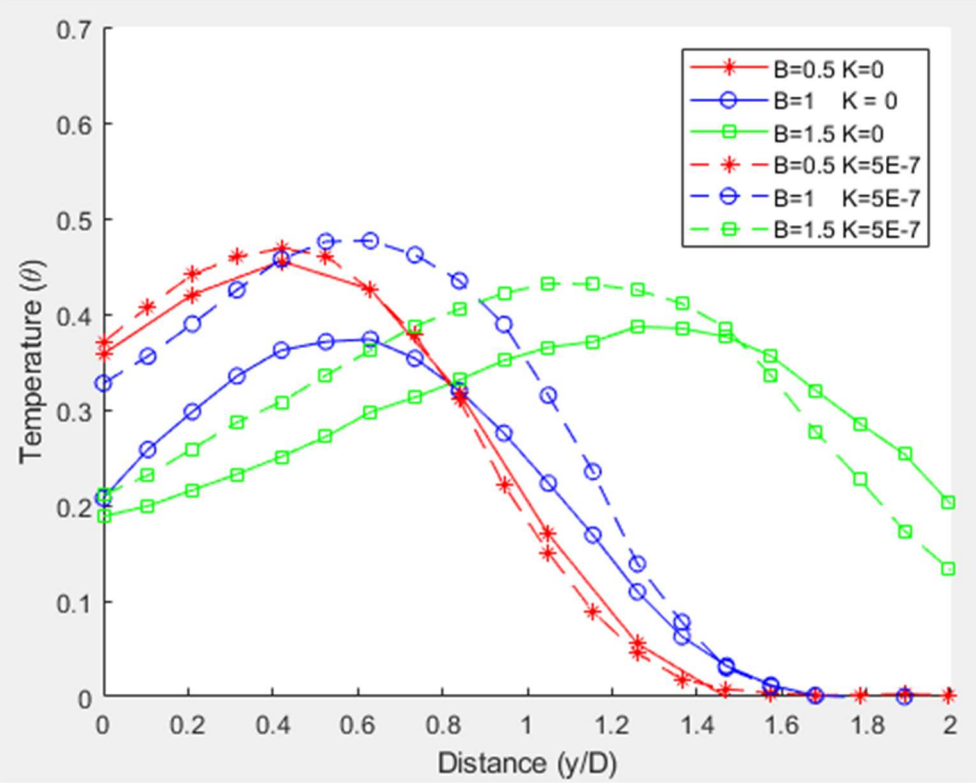

Figure 20 – Temperature Profiles, Z=0, X=7D

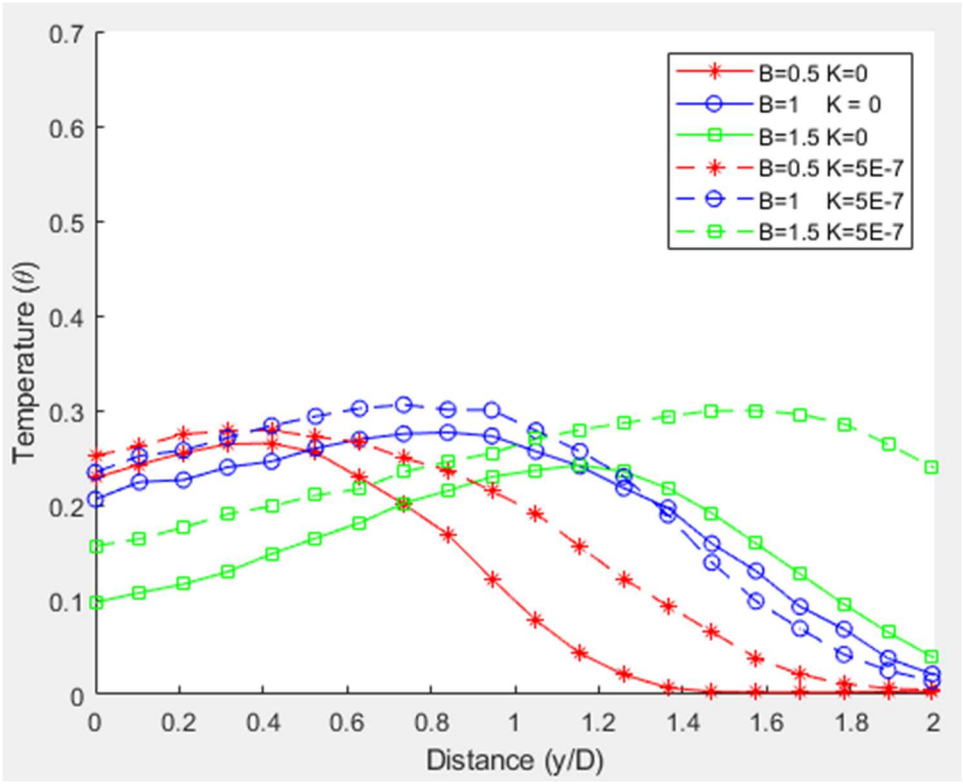

Figure 21 – Temperature Profiles at Z=0, X=12D

The center of the jets can be seen where the temperature for each scenario reaches a maximum. Most notably in Figure 19, as the blowing ratio increases, the center of the jet moves away from the test wall with increased liftoff. This is also true for distances of 7D and 12D as well. The jets in all cases were eventually turned toward the streamwise direction by the mainstream flow, but those with higher velocity are able to penetrate farther in the y direction before this turning is complete. On all of the plots, acceleration causes the jet to be shifted slightly towards the test wall, decreasing liftoff. The acceleration also moves the plots higher with regards to dimensionless temperature, which was noted previously based on the entire temperature profile grid. The lower turbulence causes less mixing with the main flow, allowing the jet to retain its higher temperatures longer.

In addition to temperature profiles, velocity profiles were measured at the same locations as the temperature profiles of Figures 19-21. These are shown in Figures 20-22 with velocity as a fraction of mainstream velocity plotted as a function of dimensionless distance from the wall in the y-direction. As before, the cases without acceleration are indicated with solid lines, while the cases with acceleration are denoted by dashed lines. The cases without any blowing are represented by the black lines.

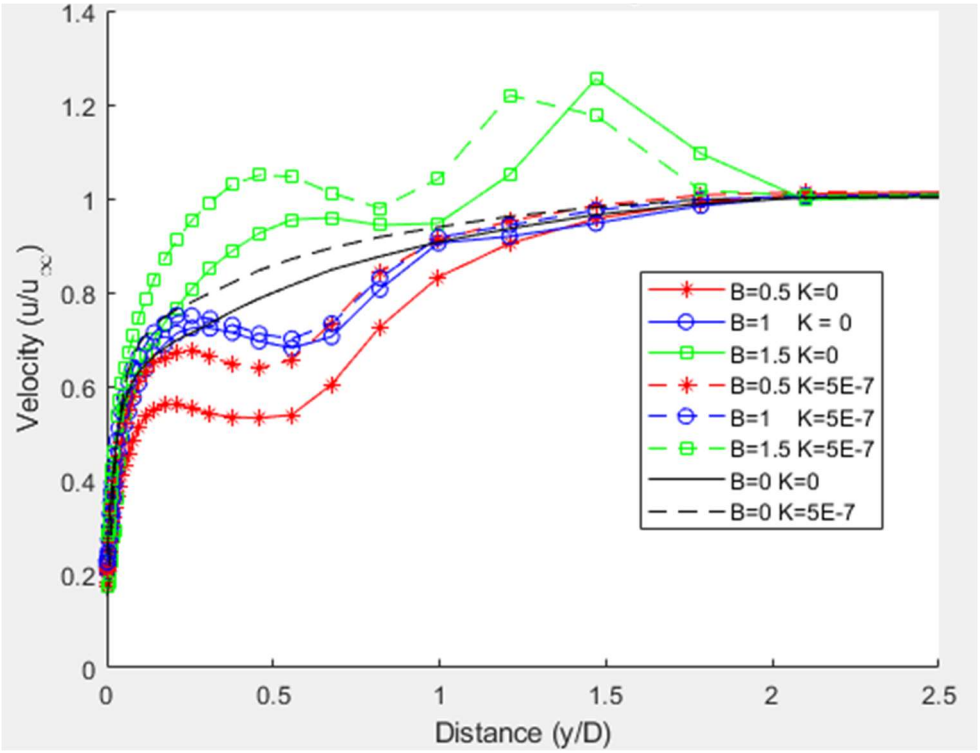

Figure 22 – Velocity Profile at X=4D

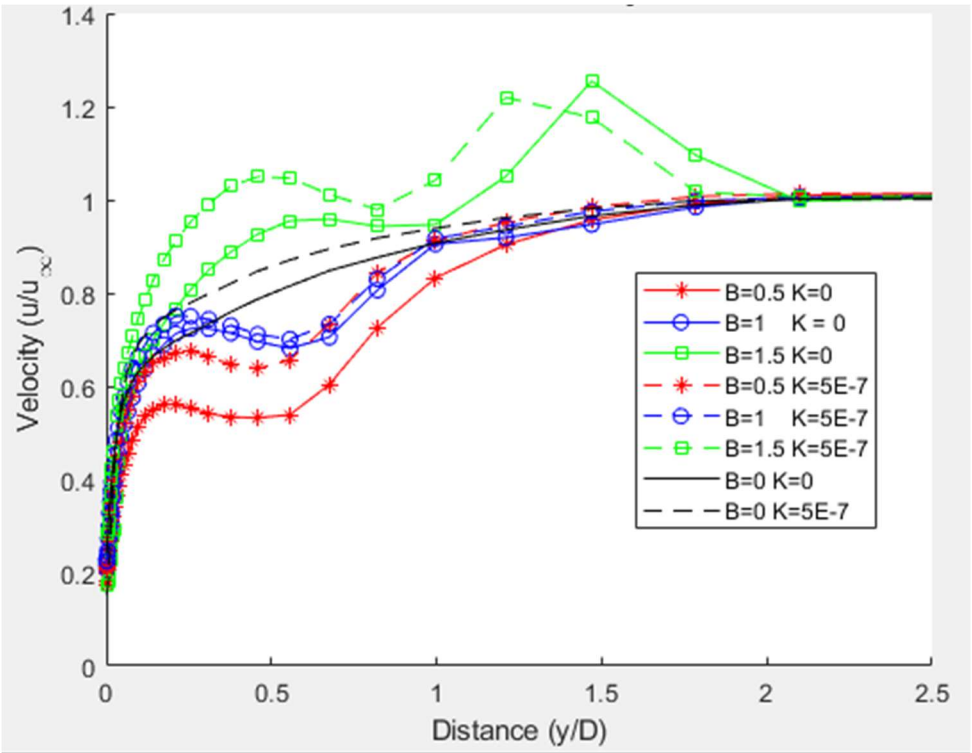

Figure 23-Velocity Profile at X = 7D

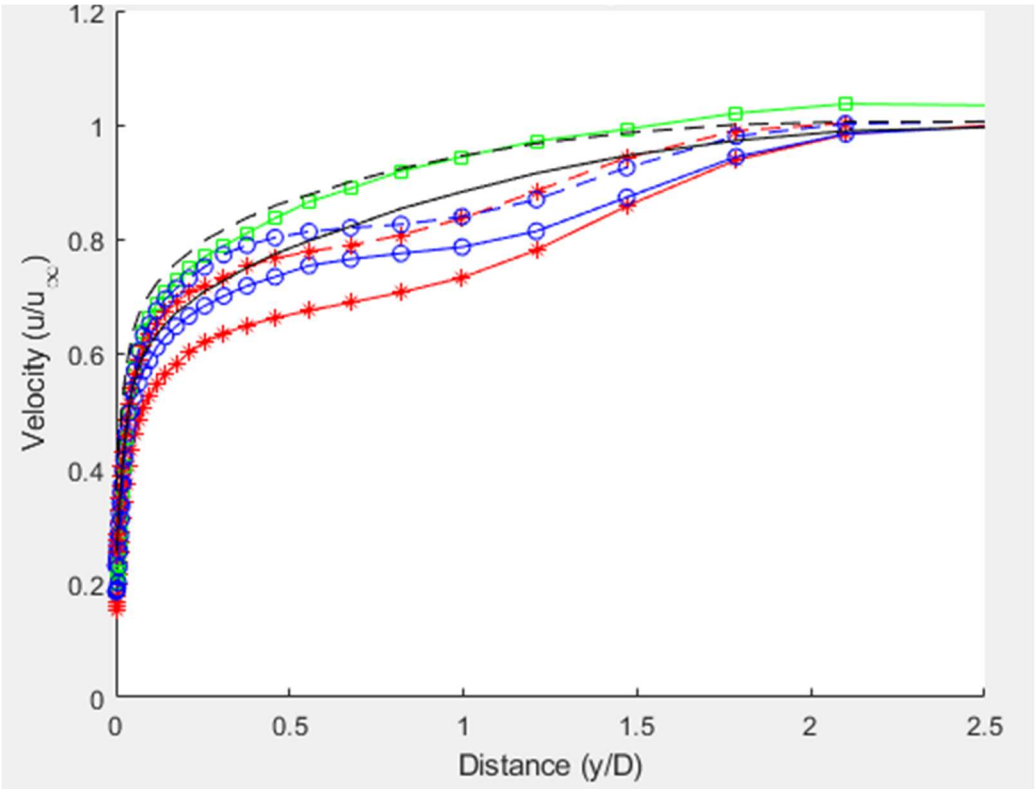

Figure 24 – Velocity Profile at X=12D

In Figure 22, the influence of the jet can be seen in the profile's first maximum. For the high blowing ratio of 1.5, the velocity through the jet increases to a point higher than the mainstream flow. This makes sense, since the jet is traveling at a higher velocity than the wind tunnel air. At lower blowing ratios, the jet is inserting lower velocity air into the main flow, causing a temporary dip in the velocity where the jet crosses the profile. The double peaks in the profiles, most visible at x/D=4, may be caused by the jets displacing the main flow, causing the mainflow to accelerate around the jet. After the profile passes through the jets, the velocity settles at the mainstream flow velocity. As the distance downstream increases, the jet effects decrease, and the profiles all begin to converge to the case without any blowing. The acceleration causes the plots to shift slightly towards the wall, indicating a thinner boundary layer thickness, causing less liftoff. The thinner

boundary layer is also shown by the quicker increase in velocity in the y direction with acceleration through all of the plots.

Finally, Figures 25-27 show turbulence levels (how much the velocity fluctuates at a certain point over time) as a function of distance from the test wall in the y-direction. The outside shear layers of the jets can be seen in the two maximums in Figure 23 for each case. The shear layers are the layers between the jet and the mainflow, where the velocity gradient can be large. This gradient causes the high turbulence. The case with a blowing ratio of 1.5 has much higher levels of turbulence close to the holes, but is noticeably more affected by the mainstream flow at farther distances from the holes. The blowing ratios of 0.5 and 1 have slightly decreased turbulence levels downstream from the hole and the jet cross-sectional area increases as well. Acceleration causes the turbulence levels to decrease, which most likely causes less mixing of the jet with mainstream flow.

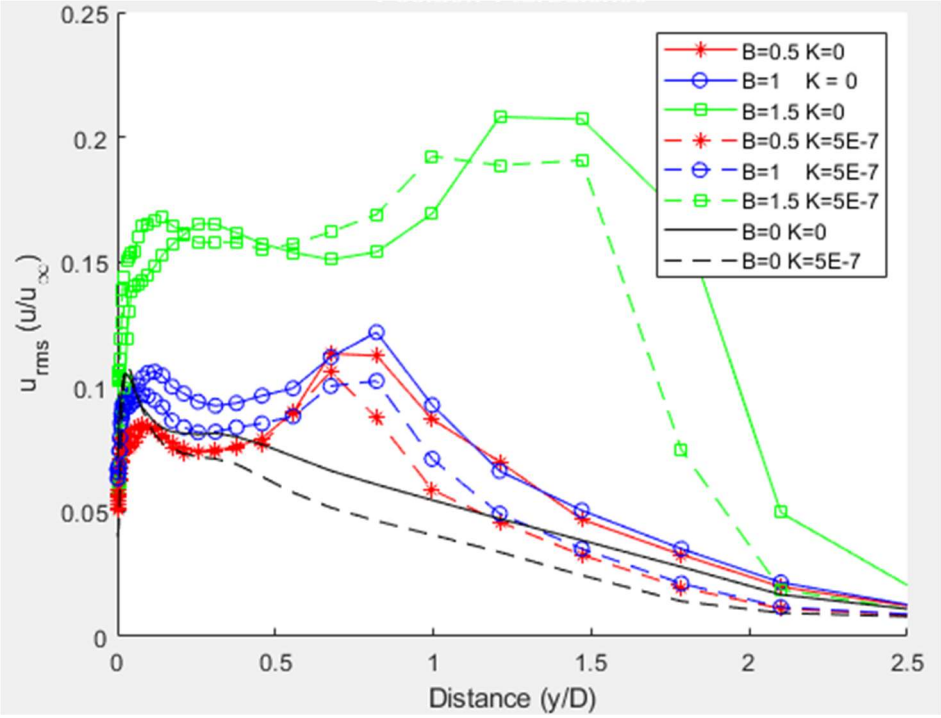

Figure 25 – Turbulence Profile at X=4D

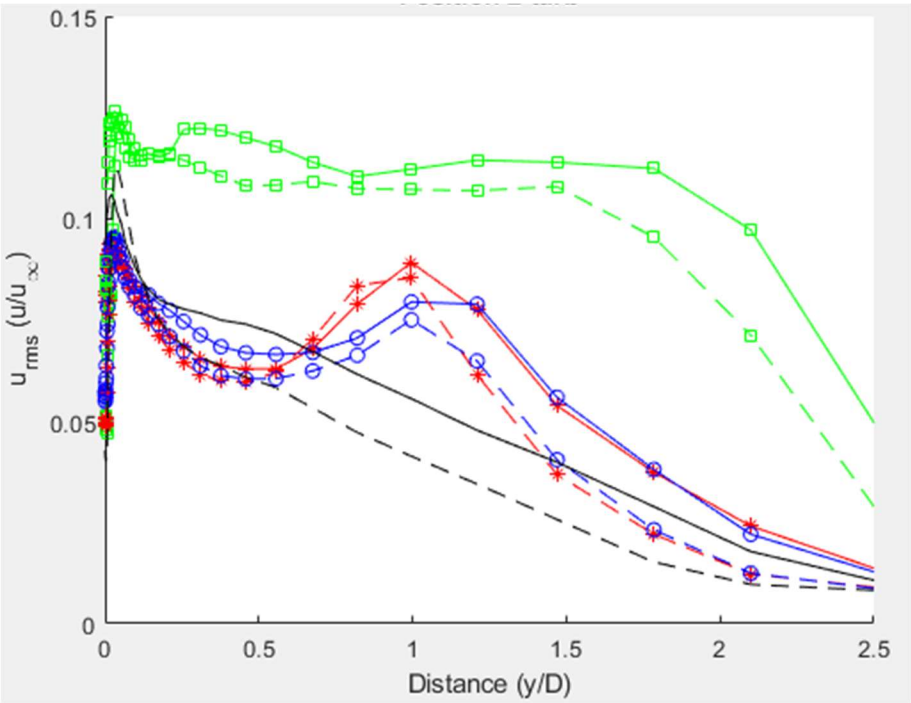

Figure 26 -Turbulence Profile at X = 7D

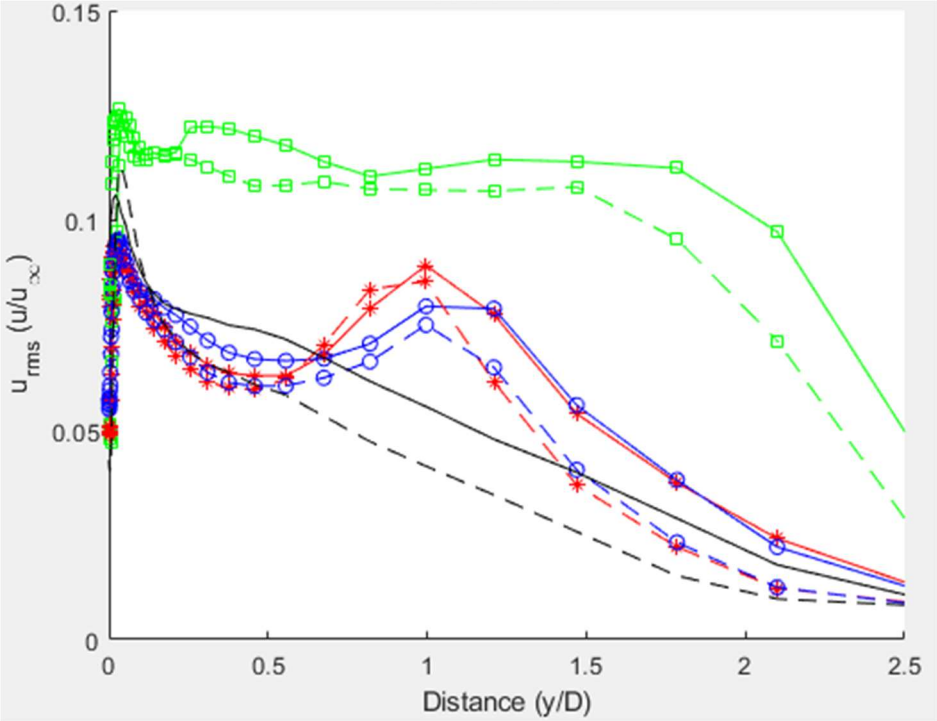

Figure 27 – Turbulence Profile at X=12D

Film Cooling Effectiveness

Figure 28 shows an example temperature reading from the infrared camera. The circle in the middle is the IR window, through which the test wall can be seen. Outside of the window, the outside wall of the test section is seen. The jets can clearly be seen on the wall below. To calculate a spanwise average, the values in the z direction were averaged at each x distance. In the spanwise average for the film cooling efficiencies, the area that was averaged surrounded only the jet in the middle of the test wall. The other active jets were used to ensure spanwise periodicity of the jet structure and effects, but were not included in the averaging.

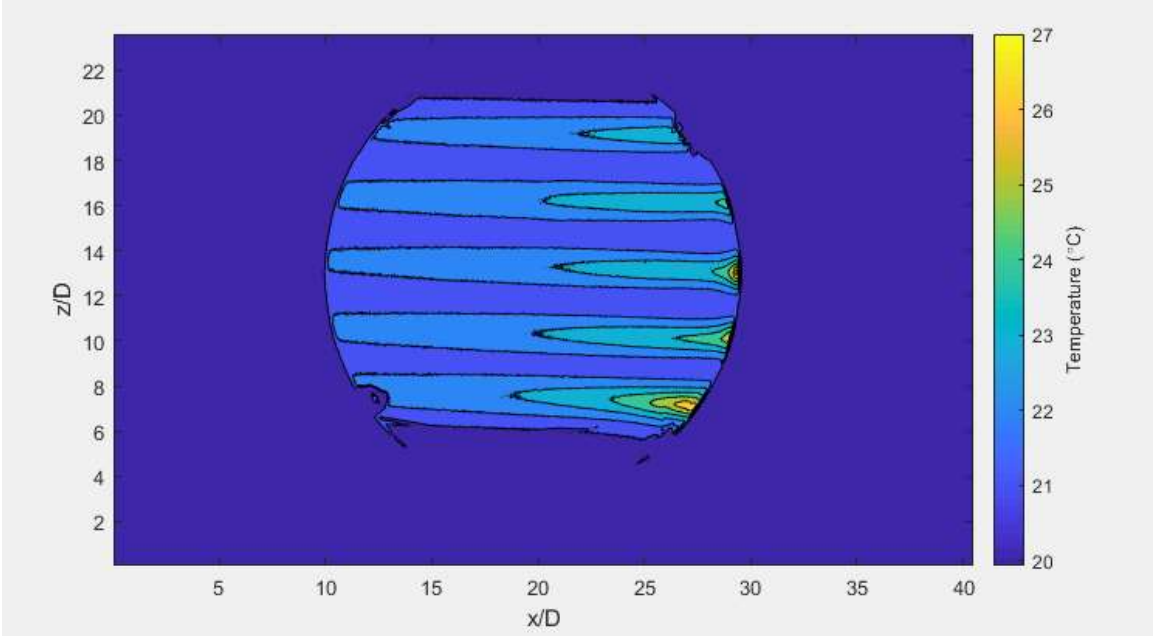

Figure 28 – Temperature on the test wall, as read directly from the infrared camera

In an effort to validate results, the experimental values gathered are compared below to the values from Coulthard et al. [14] in Figure 29. Centerline results are shown in Figure 29a, which presents the effectiveness along a streamwise line extending from the spanwise center of a hole. Figure 29b results that have been spanwise averaged across a hole spacing between

-1.5<z/D<1.5. The Coulthard results for a blowing ratio of 1 and 1.5 indicated jet liftoff and re-contact with the wall, shown by the dip in efficiency around 1D downstream of the holes. This trend is still present in the span averaged values, but much more sharply than the present study's results.

The Coulthard results reported effectiveness that was much higher than the present study. Part of the reason may be the different jet velocity profiles in the two studies. In Coulthard et al. [14], the length to diameter ratio of the jet holes was shorter than in the present study, resulting in a more uniform jet velocity distribution. The ratio of the maximum jet velocity to the bulk velocity was close to 1. In the present study, as shown in Figure 12 and Table 2, the jet velocity profiles were closer to that of fully developed turbulent pipe flow, and the ratio of the bulk velocity to maximum velocity was about 0.7. If the blowing ratio was based on the maximum velocity in the jet, the values for the present study would be 0.76, 1.36, and 1.64. Even accounting for these differences, the present results are well below the Coulthard et al. [14] results. The difference may be due to the large experimental uncertainty described above.

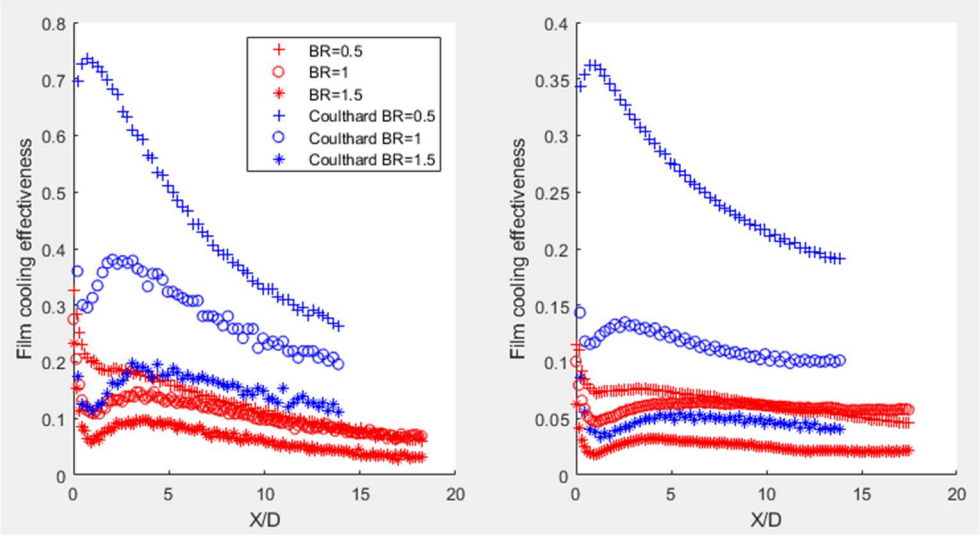

Figure a **Figure b**

Figure 29 – Compared Data for Film Cooling Effectiveness at K = 0 for Various Blowing Ratios, a is along the centerline, b is span averaged.

There is some inconclusive evidence to suggest that the high uncertainties in the temperatures arose midway through the present study. It is believed that the uncertainties in the flow temperature results of Figures 19-22 may have been lower. Studies such as Womack et al. [15] have shown that the local dimensionless temperature θ approaches the local film cooling effectiveness at y=0. The θ values at y=0 in Figure 19-22 appear to be considerably closer to the effectiveness values of Coulthard et al. [14] in Figure 29 than the present results in Figure 29. In spite of the apparent problems with the present data, the film cooling effectiveness results will still be shown below to show possible trends with acceleration. Given the uncertainty, however, the results and conclusions should be treated with caution.

Figure 30 shows the film cooling effectiveness along the wall for a blowing ratio of 0.5. The acceleration parameter increases from top to bottom in the figure. The highest film cooling effectiveness measured was 0.5 immediately following the holes. For the case without any acceleration, the maximum effectiveness was roughly 0.3, dropping to 0.1 on the centerline at about x/D = 10. At an acceleration of $K = 0.5x10^{-6}$, the film cooling effectiveness was clearly increased both near the holes and downstream of the holes. The effectiveness was 0.5 within about a quarter diameter of the hole, before falling to 0.3 at x/D=3. The effectiveness decreased to 0.1 along the centerline at a distance of about 18D. Clearly, the acceleration increased the film cooling effectiveness.

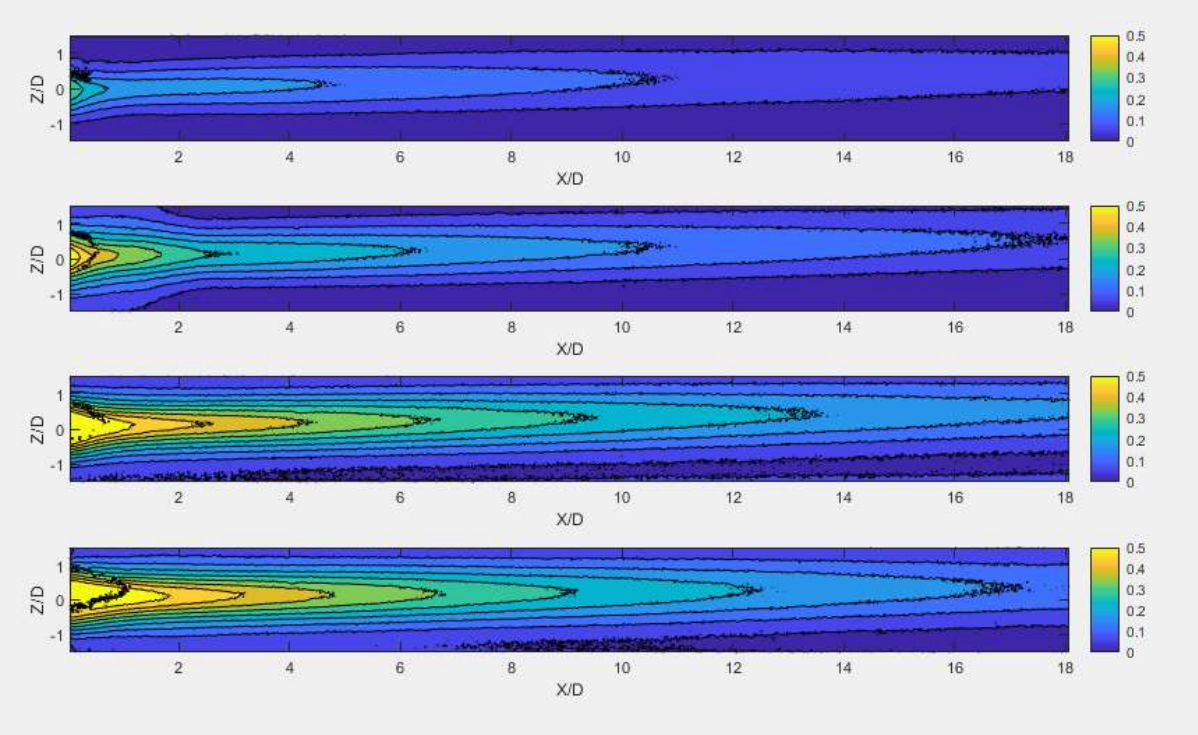

Figure 30 – Film cooling effectiveness at a blowing ratio of 0.5, from top to bottom K = 0, 0.5x10^{-6}, 1x10^{-6}, and 2x10^{-6}

Figure 31 shows film cooling efficiency as a function of streamwise distance on the test wall at a blowing ratio of 0.5 and four levels of acceleration.

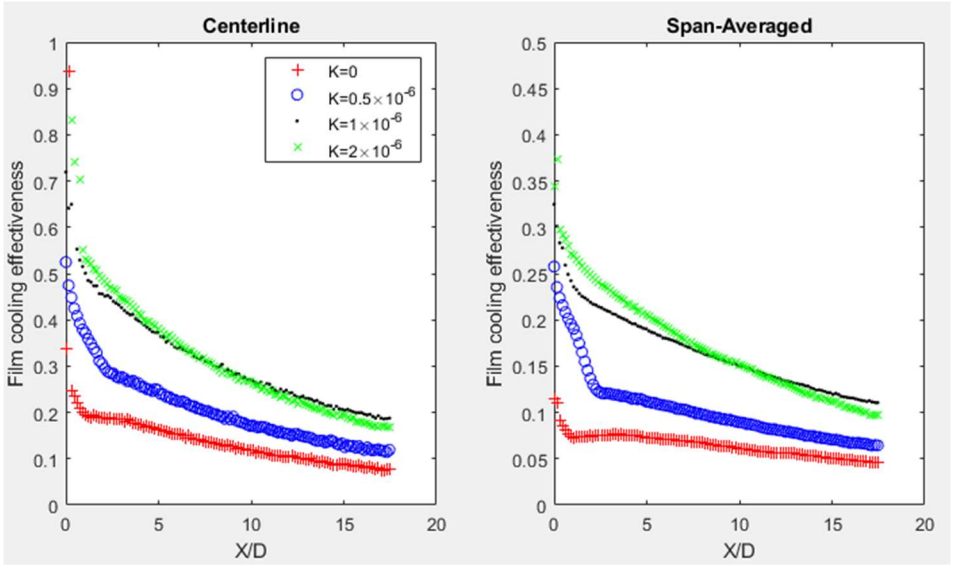

Figure a **Figure b**

Figure 31 – Film cooling effectiveness as a function of horizontal distance at a blowing ratio of 0.5, a is along the centerline, b is span averaged.

The trends from Figure 30 remain the same in the centerline – as the acceleration increases, the film cooling effectiveness overall increases. Moving down the test wall, the effectiveness decreases. Along the centerline there appears to be very little to no difference between K = 1 and 2 $x10^{-6}$ results as noted previously. However, for the span averaged data values, the acceleration of $2x10^{-6}$ has a visibly increased effectiveness over the test wall until x/D = 8, as compared to the acceleration of $1x10^{-6}$ in Figure 31.

Figure 32 shows the film cooling effectiveness along the test wall at a blowing ratio of 1. The traces of the jets in the figure do not proceed straight downstream in the x direction, but instead show a spanwise trend toward higher z as the jet moves downstream. There is also indication of motion in the z direction in Figure 30, but the trend was not as strong at the lower blowing ratio. A possible explanation may be buoyancy effects on the jets.

Because the jets are over 10 °C warmer than the main flow, the jet air is less dense. As a result, buoyancy forces would tend to push the jet upwards in the z direction, which is apparent from the contour lines in Figure 32. The buoyance forces should not be strong enough to produce this much of an effect; however, another possible explanation is slight misalignment of the holes from the streamwise direction. Misalignment would cause the effect shown, and would become stronger at higher blowing ratios.

An additional trend that can be seen is an apparent necking of the effectiveness roughly between 1 and 3D from the holes. The jet lifts off the test wall slightly, having less effect on the wall at around 1D. As the jet expands, it begins to affect the wall more strongly as “contact” is increased. The most obvious example is in the topmost plot, where K=0. Between roughly x/D = 2 and x/D = 5, the film cooling effectiveness increases along the centerline to about 0.18, as the jet begins to influence the wall more. This effect decreases as the acceleration increases, as the acceleration

pushes the jet closer to the test wall. In the bottom-most graph, this necking effect can barely be seen.

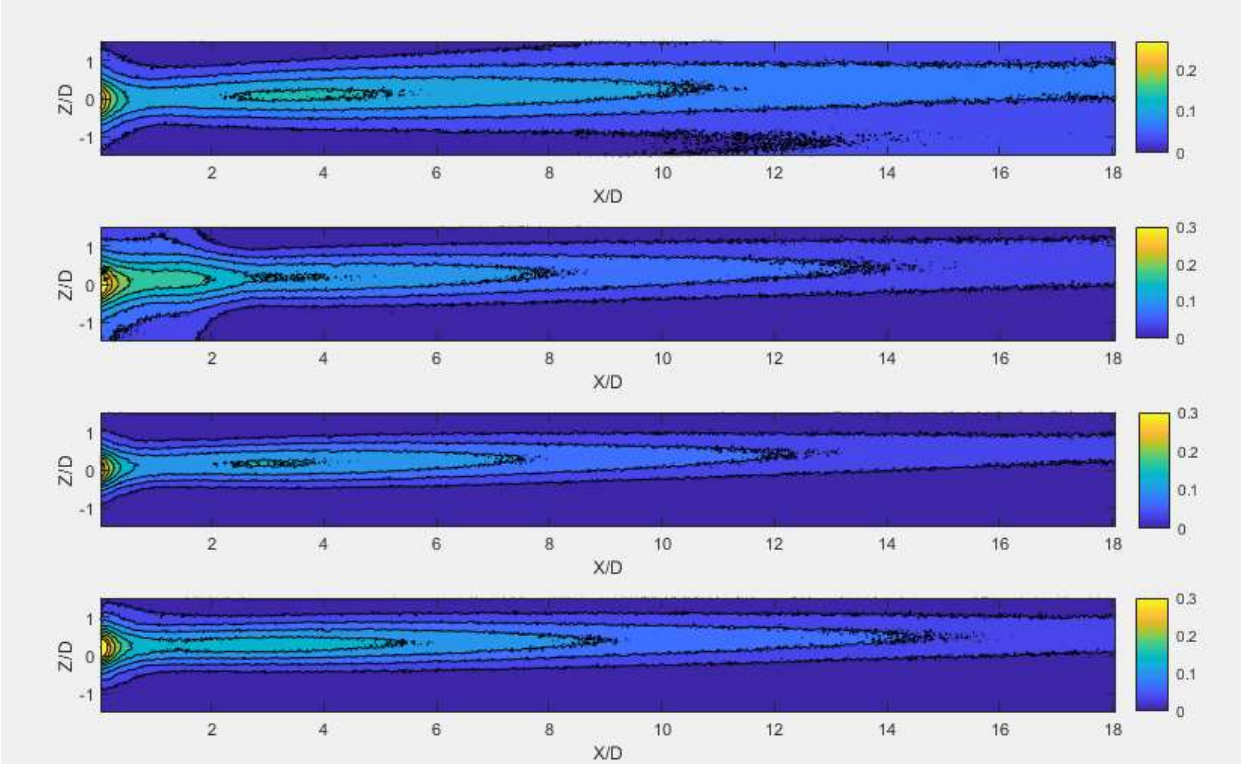

Figure 32 – Film cooling effectiveness at a blowing ratio of 1, from top to bottom K = 0, $0.5x10^{-6}$, $1x10^{-6}$, and $2x10^{-6}$

The general effectiveness at the blowing ratio of 1 is substantially lower than the effectiveness at a blowing ratio of 0.5. The effectiveness is never greater than 0.3, whereas with the lower blowing ratio of 0.5, the effectiveness was as high as 0.5.

Figure 33 shows the centerline and span averaged values for a blowing ratio of 1. For the centerline values, the effectiveness varies little with increasing the acceleration. The acceleration of K=0.5 x 10^{-6} leads to a higher span averaged effectiveness, nearly 0.05 higher than the other cases at x/D = 1. This difference can be seen in Figure 32, most noticeably between x/D = 0 and x/D = 2, where

the jet's effects are spread out in the Z direction more. A trend is difficult to distinguish in the values for this blowing ratio of 1, based on increasing acceleration.

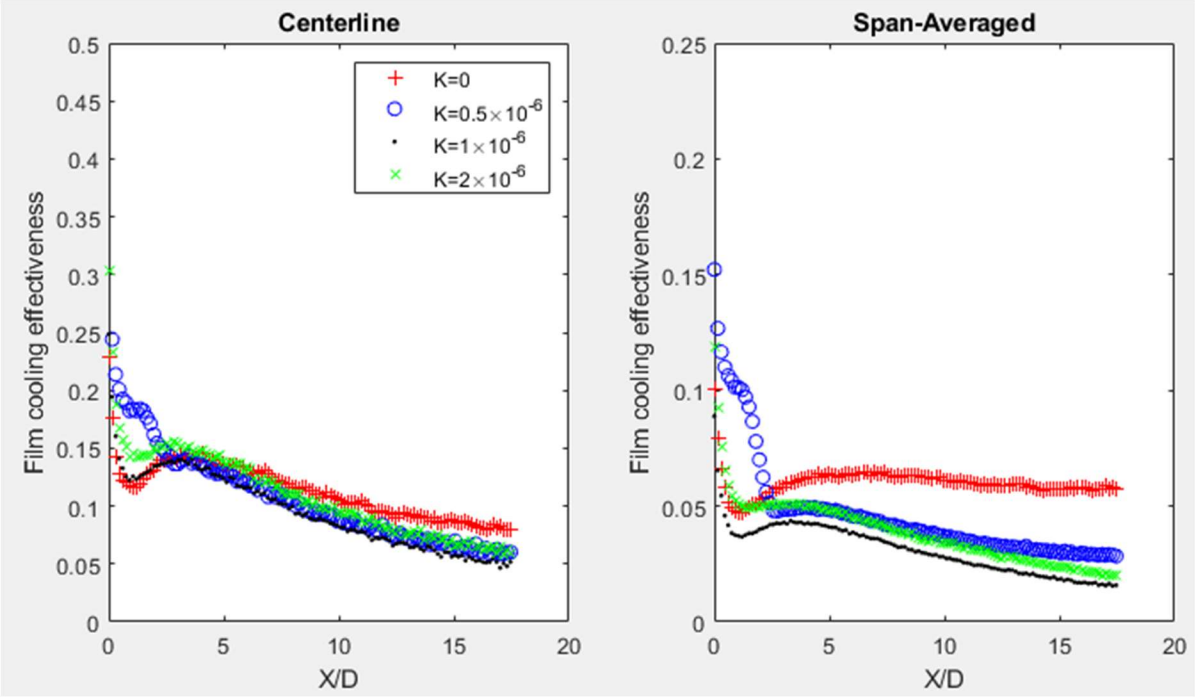

Figure a **Figure b**

Figure 33 –Film Cooling Effectiveness as a Function of Distance in the X Direction at a Blowing Ratio of 1, a is along the centerline, b is span averaged.

Figure 34 below shows the film cooling effectiveness contour plots for a blowing ratio of 1.5, with acceleration increasing from the top plot to the bottom. The same trend found at a blowing ratio of 1 can be seen for the acceleration of $K=0.5x10^{-6}$, where the jet experiences less liftoff and increases the temperature of the wall from x/D = 0 to 2 from the holes. By the time the jet reaches x/D = 3, the effectiveness is stronger for the K=0 case. Otherwise, there is not a large variation with effectiveness as acceleration increases.

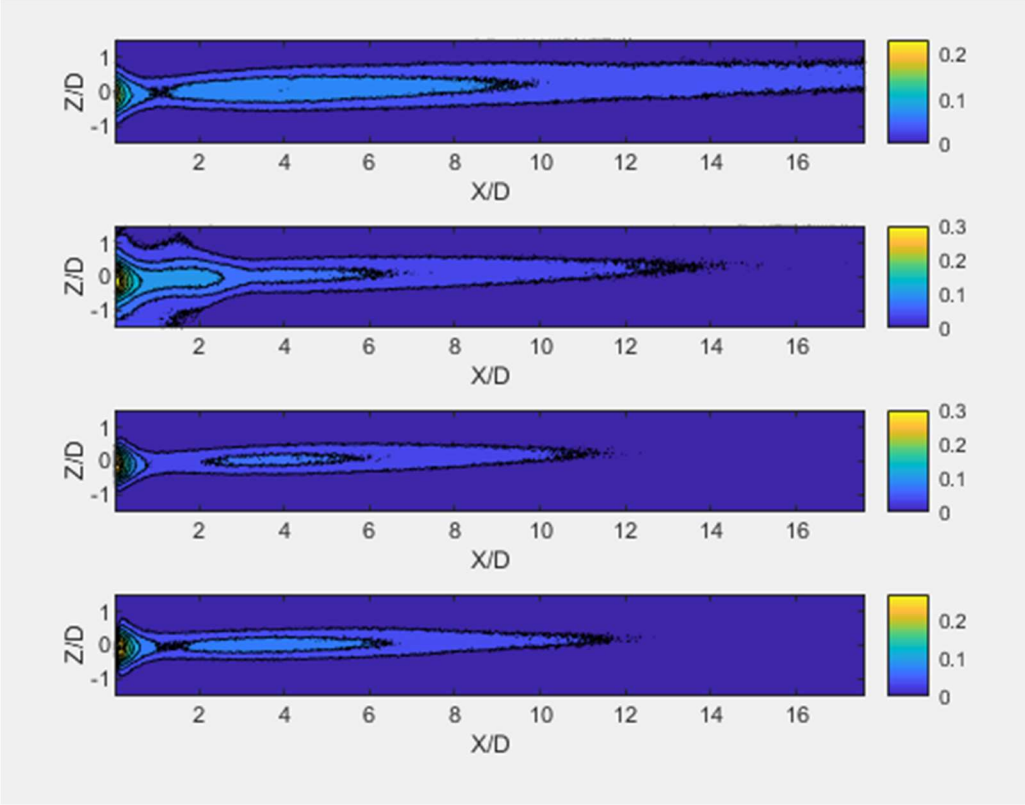

Figure 34 – Film cooling effectiveness at a blowing ratio of 1.5, from top to bottom K = 0, $0.5x10^{-6}$, $1x10^{-6}$, and $2x10^{-6}$

Figure 35 below shows the centerline and span-averaged values for effectiveness moving in the x direction along the test wall. The shape of the plots look very similar to the plots in Figure 33 for a blowing ratio of 1, though their magnitude has been decreased. The highest film cooling effectiveness is found at the acceleration of K=$0.5x10^{-6}$ initially, but as reported above the effectiveness is highest with K=0 after roughly 12D. The centerline values are all very similar again, implying that after a certain blowing ratio maximum, changing the acceleration does not influence film cooling effectiveness enough to draw conclusions about its impact.

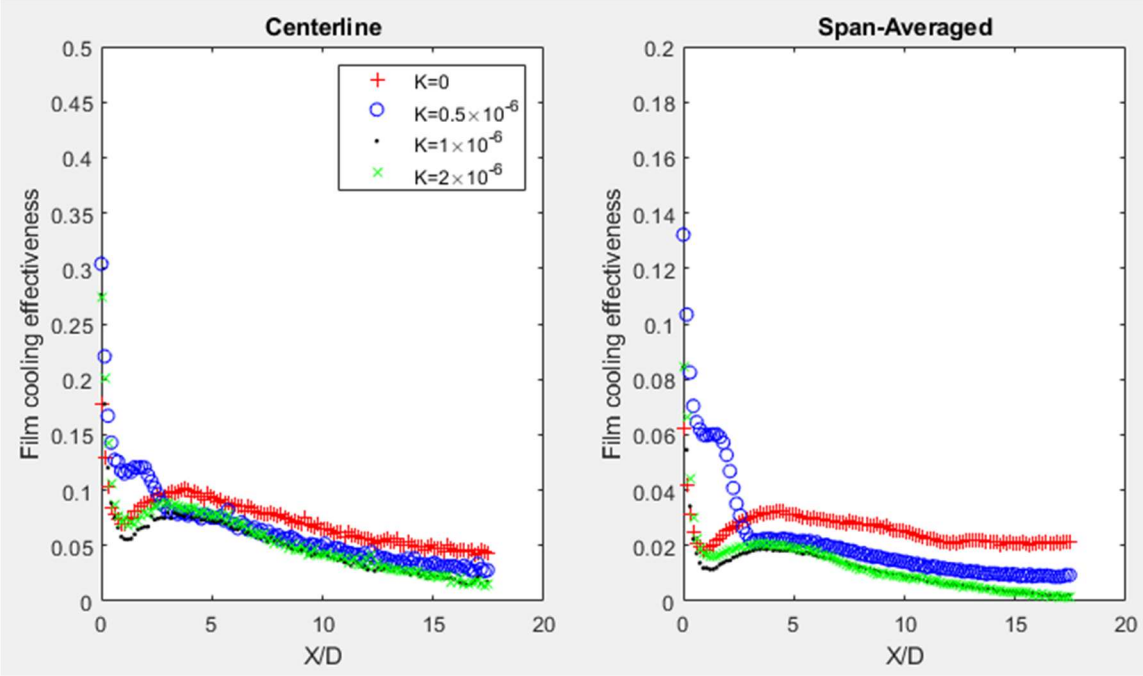

Figure a **Figure b**

Figure 35 –Film Cooling Effectiveness as a Function of Distance in the x Direction at a Blowing Ratio of 1.5, a is along the centerline, b is span averaged.

Figure 36 below shows the centerline and span averaged film cooling efficiency values as a function of distance in the x direction for various blowing ratios when the acceleration parameter K = 0. As expected, as blowing ratio increases, the effectiveness decreases due to greater jet liftoff. This trend is generally consistent at all levels of acceleration. With regards to centerline effectiveness, all blowing ratios experience a dip in effectiveness between 0 and 1D from the hole, due to the jet lifting off of the test wall. The effectiveness for the blowing ratio 0.5 decreases more quickly than for the ratio of 1, reaching the same value around x/D = 13. For the span-averaged values, the effectiveness for each blowing ratio has a minimum around x/D = 5, after which they slowly increase as the jet spreads out and influences more of the test wall. In general, the differences in effectiveness between the blowing ratios are much smaller without acceleration than with it.

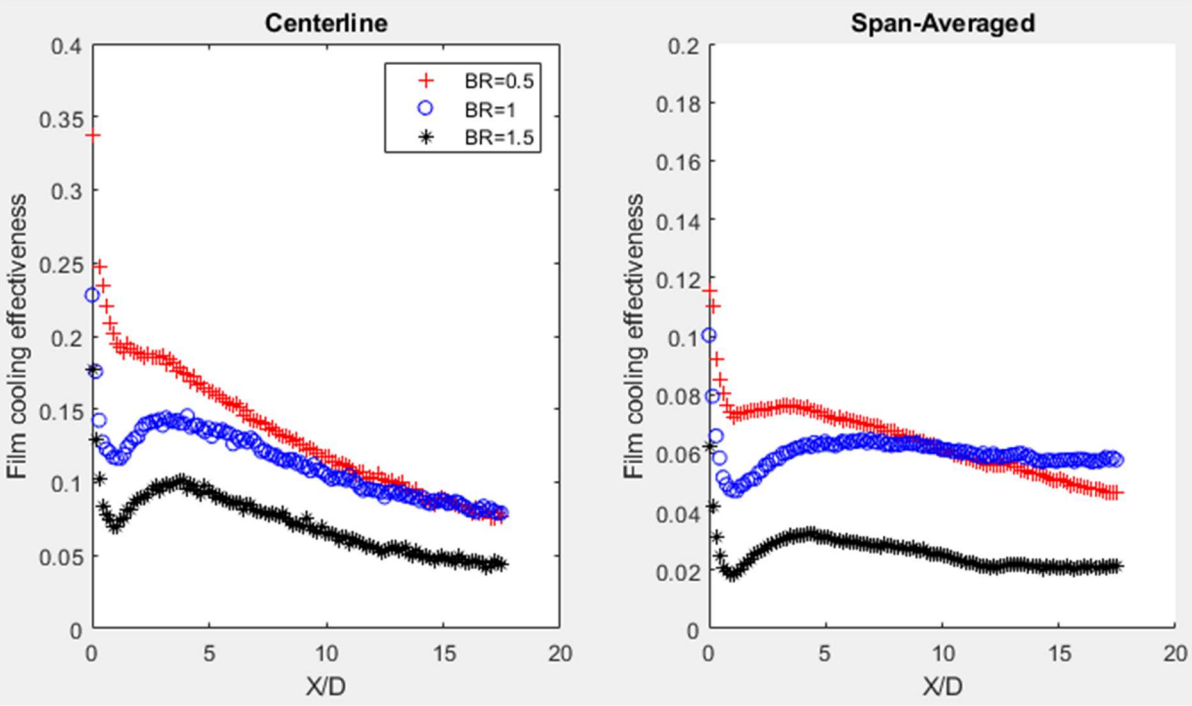

Figure a **Figure b**

Figure 36 –Film Cooling Effectiveness for Various Blowing Ratios as Functions of Distance in the X Direction, K=0, a is along the centerline, b is span averaged.

Figures 37 through 39 below show cooling effectiveness at the three different acceleration parameter settings. Uniquely, the film cooling effectiveness for the acceleration of $K=0.5x10^{-6}$ shows a different shape for the span-averaged effectiveness. Rather than decreasing and then leveling out or slightly increasing like the other acceleration cases, the curves have a shallower slope from roughly x/D = 3 to 7. In the case of B= 1.5, the curve flattens out completely over this area. This flattening indicates that at this specific acceleration, the jet hugs the test wall more, rather than lifting off early as in the other cases. For the centerline effectiveness, this “hump” can be seen shortly after the holes to about 3D.

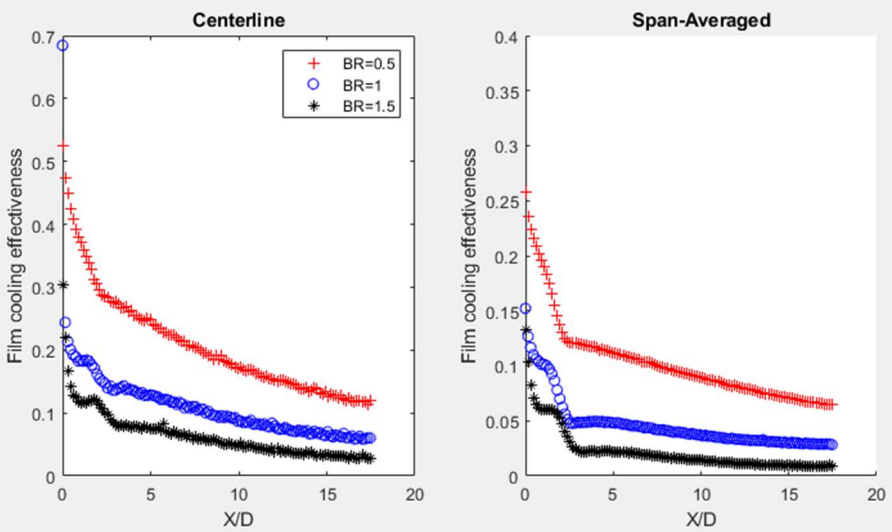

Figure a **Figure b**

Figure 37 - Film Cooling Effectiveness for Various Blowing Ratios as Functions of Distance in the x Direction, $K=0.5x10^{-6,}$ a is along the centerline, b is span averaged.

Figures 37-39 look very similar, where an increasing blowing ratio decreases the film cooling effectiveness. Other than ensuring that these expected trends exist, the comparisons for different blowing ratios are not very helpful in determining how acceleration affects the film cooling.

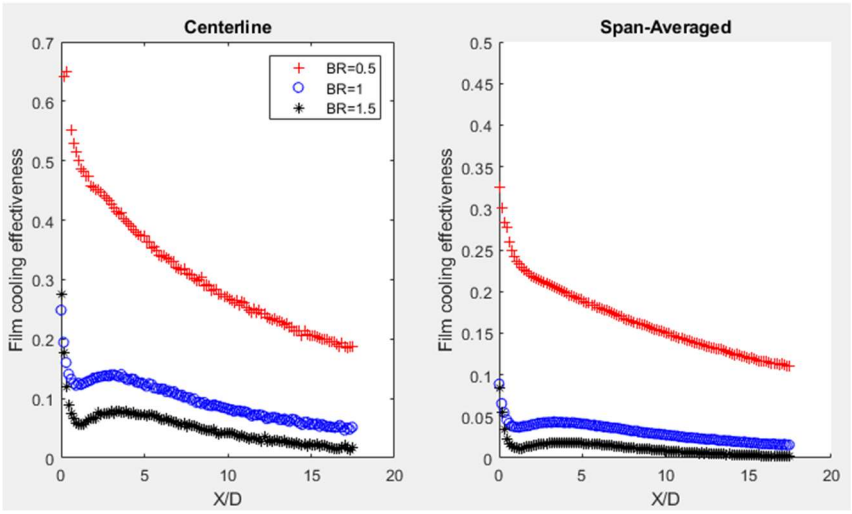

Figure a **Figure b**

Figure 38 - Film Cooling Effectiveness for Various Blowing Ratios as Functions of Distance in the x Direction, $K=1x10^{-6}$, a is along the centerline, b is span averaged.

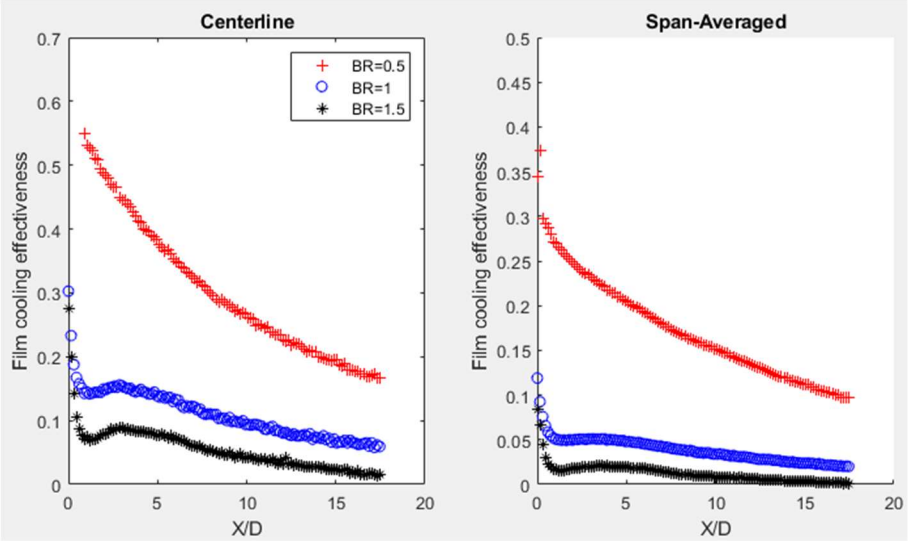

Figure a **Figure b**

Figure 39 - Film Cooling Effectiveness for Various Blowing Ratios as Functions of Distance in the x Direction, $K=2x10^{-6}$, a is along the centerline, b is span averaged.

Conclusions

Film cooling in gas turbine engines is extremely complicated, and this experiment sought to determine the effect that accelerating flow on the turbine blade has on film cooling. Previous experiments have compared film cooling with and without accelerating flow, but no one has observed heat transfer, film cooling efficiency, and flow with different levels of acceleration. Although this study was unable to determine accurate heat transfer rates and had large uncertainty in film cooling effectiveness, general trends were observed. As acceleration increases, the film cooling effectiveness experienced by the test wall also increases. In general, acceleration appears to cause less liftoff of the film cooling jets, increasing their effect on the test wall. The acceleration also leads to less mixing of the jet with the mainstream flow, allowing it to retain its structure and temperature longer. At higher blowing ratios, acceleration has a smaller effect on the film cooling efficiency because the jet lifts off the test wall quickly and has little influence on heat transfer along the test wall.

References

1. Moran, M. and Shapiro, H., 2006, "Fundamentals of Engineering Thermodynamics," 5th ed, John Wiley & Sons LTD.

2. Mom, A.J.A., 2013, "Introduction to Gas Turbines," Modern Gas Turbine Systems. P. Jansohn, ed., Woodhead Publishing, Cambridge, United Kingdom, pp 3-20.

3. Han, Je-Chin, 2004 "Recent Studies in Turbine Blade Cooling," International Journal of Rotating Machinery, **10**, pp 443-457.

4. Achyara, S. and Mahmood, G., 2006, "Turbine Blade Aerodynamics," The Gas Turbine Handbook, U.S. Department of Energy.

5. Kandil, M., and Elnady, A., 2017. "Performance of GOE-387 Airfoil Using CFD," International Journal of Aerospace Sciences, **5**, pp 1-7.

6. Vinton, K., Watson, T., Wright, L., and Crites, D., 2016, "Combined Effects of Freestream Pressure Gradient and Density Ratio on the Film Cooling Effectiveness of Round and Shaped Holes on a Flat Plate," ASME paper GT2016 - 1223, ASME Turbo Expo 2016: Turbomachinery Technical Conference and Exposition proceedings.

7. Lutum, E., Wolfersdorf, J., Semmler, K., Dittmar, J., and Weigand, B., 2001, "An experimental investigation of film cooling on a convex surface subjected to favourable pressure gradient flow," International Journal of Heat and Mass Transfer, **44**, pp 939-951.

8. Coletti, F., Elkins, C., and Eaton, J., 2013, "An inclined jet crossflow under the effect of streamwise pressure gradients," Exp Fluids, **54**, pp 1589-1605.

9. Maiteh, B. Y., and Jubran, B. A., 2004, "Effects of pressure gradients on film cooling effectiveness from two rows of simple and compound angle holes in combination," Energy Conversion and Management, **45**, pp 1457-1469.

10. Schmidt, D. L. and Bogard, D. G., 1995, "Pressure Gradient Effects on Film Cooling," ASME paper 95-GT-18, ASME 1995 International Gas Turbine and Aeroengine Congress and Exposition, pp 1-8.

11. Qpedia, 2007, "Understanding Hot-Wire Anemometry," Advanced Thermal Solutions, Inc, pp. 13. Last accessed April 7, 2020. URL: http://www.qats.com/Download/Qpedia_Dec07_Understanding%20hot%20wire%20amemometry.ashx

12. Omega Engineering, August 22, 2018, "Thermocouples" Last accessed April 13, 2020. URL: https://www.omega.com/en-us/resources/thermocouples

13. Infrared Thermography Specialists, 2018, "What is Infrared Radiation?" Last accessed November 14, 2018. URL: https://ipi-infrared.com.au/how-do-infrared-cameras-work/

14. Coulthard, S., Volino, R., and Flack, K., 2006, "Effects of Unheated Started Lengths in Film Cooling Experiments," ASME Journal of Turbomachinery, **128**, pp 579-588.

15. Womack, K., Volino, R., and Schultz, M., 2008, “Measurements in Film Cooling Flows with Periodic Wakes,” ASME Journal of Turbomachinery, **130**, pp 1-13.